Implementation of cell-free biological networks at steady state

Henrike Niederholtmeyer, Viktoria Stepanova, and Sebastian J. Maerkl[1]

Institute of Bioengineering, School of Engineering, École Polytechnique Fédérale de Lausanne, CH-1015 Lausanne, Switzerland

Edited by Jack W. Szostak, Howard Hughes Medical Institute and Massachusetts General Hospital, Boston, MA, and approved August 27, 2013 (received for review June 12, 2013)

Living cells maintain a steady state of biochemical reaction rates by exchanging energy and matter with the environment. These exchanges usually do not occur in in vitro systems, which consequently go to chemical equilibrium. This in turn has severely constrained the complexity of biological networks that can be implemented in vitro. We developed nanoliter-scale microfluidic reactors that exchange reagents at dilution rates matching those of dividing bacteria. In these reactors we achieved transcription and translation at steady state for 30 h and implemented diverse regulatory mechanisms on the transcriptional, translational, and posttranslational levels, including RNA polymerases, transcriptional repression, translational activation, and proteolysis. We constructed and implemented an in vitro genetic oscillator and mapped its phase diagram showing that steady-state conditions were necessary to produce oscillations. This reactor-based approach will allow testing of whether fundamental limits exist to in vitro network complexity.

synthetic biology | cell-free protein synthesis | computational biology | minimal artificial cell

Instead of complex and ill-characterized cellular hosts, in vitro systems have recently become popular alternatives for implementing synthetic networks. In vitro systems can be completely defined, easily manipulated, interrogated, and have been used to study a number of biological phenomena. For example, periodic temporal patterns were observed in systems based on nucleic acid synthesis and degradation (1, 2), and ordered spatial patterns were created from purified cell division regulators (3). In vitro transcription and translation (ITT)-based systems should, in principle, be able to use all regulatory functionalities found in living cells. Reconstituted, defined ITT systems like the PURE mix (4), are particularly appealing for bottom-up synthetic biology. A number of recent examples show that various genetic (5–10) and metabolic (11) networks can be implemented in ITT systems. Genetic network complexity has, however, been limited to genetic cascades, where the output of one stage acts on the next stage, whereas examples of positive and negative feedback have been basic (8, 9, 12). The main limitation to network complexity in vitro derives from its batch reaction format. In batch, synthesis rates decrease as precursors are consumed, enzymatic activities degrade, and reaction products accumulate. This rapid approach to chemical equilibrium severely limits network size. In addition, negative feedback is particularly difficult to implement, because regulators from earlier stages are not removed. The implementation of active degradation mechanisms for RNA and proteins (13) could solve the problem of product removal, and synthesis times can be increased by using reactors that allow an exchange of small molecules between the ITT mix and a feeding solution. Large-volume continuous flow and exchange systems were developed to increase the amounts of protein produced by ITT systems and are based on diffusion of small molecules through ultrafiltration membranes (14, 15). Scaled down versions of reactors using similar principles were more recently developed to increase throughput and minimize cost (16, 17). Cell-free genetic networks have, however, not yet profited from the full potential of continuous reaction conditions, although protein synthesis in a functionalized phospholipid vesicle surrounded by a feeding solution (18) and a two-stage genetic activation cascade in a dialysis system yielded promising results (9).

Results

Steady-State Transcription and Translation in Microfluidic Nanoreactors. To enable the implementation of complex genetic networks in vitro, we developed a microfluidic device in which ITT proceeds at steady state for extended periods of time. Our microfluidic device contains eight independent 33-nL reactors (*SI Appendix*) and functions similarly to previous devices (19–21). Dilutions occurred in discrete steps, where each dilution step added fresh ITT mix and template DNA, displacing part of the old reaction volume (Fig. 1*A*). Dilution rates could be precisely tuned by changing the volume displaced per dilution step in a range of 10–40% of reactor volume. The time interval between dilution steps was kept constant at 15 min (*SI Appendix*). These exchanges resulted in dilution rates of 0.4–2 h^{-1}. To enable long-term reactions, we cooled the ITT mix off chip to 6 °C, while keeping the on-chip reaction temperature at 37 °C. Fluorescent reporters allowed us to determine DNA, mRNA, and protein concentrations in real time (22) and a computer program controlled all device and imaging operations (Fig. 1*B* and *SI Appendix*).

We used a reaction rate model to describe the process of transcription and translation (22–24). We measured the reaction rate parameters that characterize an ITT batch reaction and added the dilution steps that replace fractions of the reactor volume with new reaction mix with full synthesis activity (Fig. 1*C*

Significance

Transcription and translation can be performed in vitro, outside of cells, allowing the assembly of artificial genetic networks. This bottom-up approach to engineering biological networks in a completely defined and minimal environment is instructive to define the rules and limitations of network construction. It is, however, still challenging to implement complex genetic networks in vitro because the reactions are usually performed in a batch format, where reaction products accumulate and synthesis rates decline over time. Here, we addressed this problem by developing a microfluidic device to perform in vitro transcription and translation reactions in continuous mode, where synthesis rates stay constant. This allowed us to build and implement a genetic oscillator that showed sustained oscillations for extended periods of times.

Author contributions: H.N. and S.J.M. designed research; H.N. and V.S. performed research; H.N. and S.J.M. analyzed data; and H.N. and S.J.M. wrote the paper.

The authors declare no conflict of interest.

This article is a PNAS Direct Submission.

Freely available online through the PNAS open access option.

[1]To whom correspondence should be addressed. E-mail: sebastian.maerkl@epfl.ch.

This article contains supporting information online at www.pnas.org/lookup/suppl/doi:10.1073/pnas.1311166110/-/DCSupplemental.

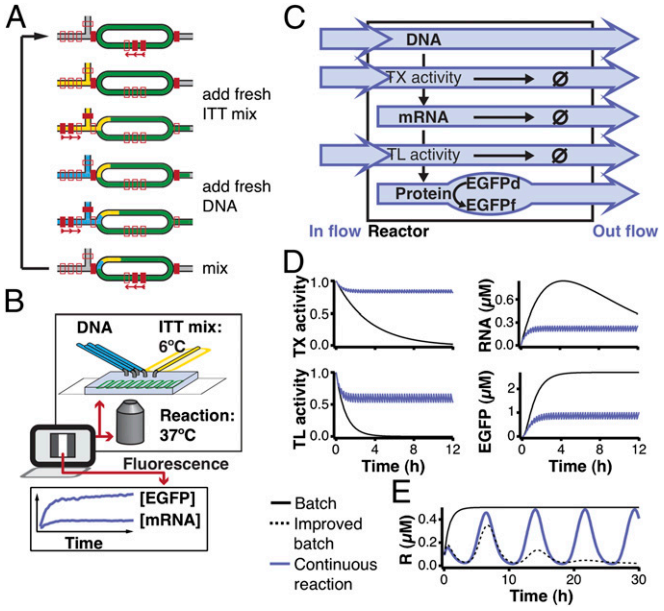

Fig. 1. ITT under steady-state conditions. (*A*) Function of a microfluidic nanoreactor for continuous ITT. At each dilution step, the supply channel is flushed with fresh reagent. A peristaltic pump meters a specific volume into the reaction ring. After both ITT mix and DNA have been added, another peristaltic pump mixes the reaction. (*B*) Experimental setup and analysis. (*C*) Model of EGFP synthesis in the reactor. Relative transcriptional (TX) and translational (TL) activities decrease at constant rates. In the continuous reaction (blue arrows), all modeled species are diluted at a constant rate, and DNA as well as relative TX and TL activities are replaced at the same rate. (*D*) Model predictions for a batch and a continuous reaction. Predictions were for 18.3 nM DNA and dilutions of 32% every 15 min. (*E*) Model of the repressilator (25) under three reaction conditions (*SI Appendix*). We show the concentration of one of the repressor proteins (R).

and *SI Appendix*). During continuous reaction, synthesis rates reach a steady state, where the rate at which activities decrease is balanced by the inflow rate of fresh reaction mix. Consequently, RNA and protein concentrations also reach steady-state levels (Fig. 1*D*). On the basis of our model, a genetic system such as the repressilator (25) would not oscillate in a batch reaction. Improvements like degradation mechanisms for mRNA and protein, as well as elongated synthesis times (9, 13, 18), could possibly lead to a few damped oscillations in batch, whereas sustained oscillations can only be obtained under continuous conditions (Fig. 1*E*).

We performed protein synthesis reactions in vitro, generating EGFP from a linear DNA template regulated by a T7 promoter at dilution rates comparable to bacterial doubling times between 20 and 104 min (Fig. 2*A*). We achieved dilution-dependent steady-state mRNA and protein levels for 30 h (Fig. 2*B*). Independent of dilution rate, DNA template concentration remained constant in all conditions (*SI Appendix*, Fig. S1). When we momentarily stopped the flow of fresh reagents, RNA and protein concentrations increased and returned to their previous steady-state levels when dilution was resumed (Fig. 2*C*). To demonstrate the dynamic nature of synthesis and dilution, we switched between periods where DNA template or water was added (Fig. 2*D*). This led to continuously changing DNA template concentrations with RNA and protein concentrations oscillating with a slight delay. Our model accurately captured these dynamic changes.

Implementation of Regulatory Mechanisms. We implemented a number of regulators, acting transcriptionally, translationally, and posttranslationally, under steady-state conditions. We transiently expressed the regulators to allow comparison of RNA and protein concentration of the reporter in the presence and absence of the regulator in one experiment (Fig. 3). We implemented transcriptional activation by expressing T3 RNA polymerase (T3RNAP) or sigma factor 70 (σ^{70}) in the presence of the *Escherichia coli* RNAP core enzyme and EGFP under control of their respective promoters. Expression of either protein increased RNA concentration from undetectable levels to ∼150 and 18 nM for T3RNAP and *E. coli* RNAP, respectively, and also increased EGFP concentration in the expected manner (Fig. 3*A*). Transcriptional repression by the transcriptional repressor TetR reduced transcription of promoters expressed by three different polymerases (T3, T7, and *E. coli* RNAP). Coexpression of *tetR* reduced RNA levels to 30%, 50%, and 40% of their unrepressed levels for T3, T7, and *E. coli* RNAP, respectively. These changes of mRNA concentration consequently led to a decrease in EGFP levels (Fig. 3*B*). We implemented translational activation using two regulator RNAs that were previously used in vivo to induce mRNA translation by transactivation and stop codon suppression (Fig. 3*C*) (26, 27). In transactivation, a transactivator RNA modifies mRNA secondary structure of a *cis*-repressed RNA, making the ribosomal binding site accessible (26). For stop codon suppression, we used the amber suppressor tRNA encoded by *supD* allowing read through of a UAG stop codon (27), which was located immediately after the start codon of the EGFP gene. Aminoacylation of the tRNA with serine required no additives to the ITT system as both enzyme and amino acid are present. These mechanisms led to an increase in EGFP concentration from undetectable levels to 14 and 35 nM, whereas RNA concentrations remained high in the presence and absence of the regulator RNA (expression of *supD* reduced RNA concentration by about 10–20%, Fig. 3*B*). To quantify the effect of both activators on translation of their respective reporter mRNAs, which were synthesized at different concentrations, we used the model of EGFP ITT to determine the ratio of observed to expected EGFP concentration for the measured mRNA concentration. According to this analysis, translation efficiency was 1.4% for transactivation and 2.8% for stop codon suppression (*SI Appendix*, Fig. S2). Finally, we successfully implemented protein degradation by reconstituting the ATP-dependent protease ClpXP (a large 700- to 800-kDa multisubunit complex) (28). Degradation of GFP targeted for recognition by AAA^+ proteases such as ClpXP has been shown in cell extracts, where these proteases are naturally present (13). Here, we functionally expressed the protease in vitro and showed that it specifically degraded EGFP fused with the ssrA degradation tag. In the presence of ClpXP, steady-state EGFPssrA concentration decreased by about 80% (Fig. 3*D*). Again, we calculated expected EGFP concentrations from the measured mRNA concentrations, which decreased when ClpX and ClpP were expressed, to determine if EGFP decrease was indeed caused by protein degradation. Only in the case of ssrA-tagged EGFP did we observe a significant decrease of observed to expected EGFP when both protease subunits were expressed (*SI Appendix*, Fig. S2).

An in Vitro Genetic Oscillator. Using three regulators from this toolbox, we built a genetic oscillator based on a positive feedback and delayed negative feedback architecture (1, 2) (Fig. 4*A*). In our oscillator network, T3RNAP induces its own expression, which constitutes the positive feedback loop. The same polymerase also transcribes the *supD* and *tetR* genes to produce amber suppressor tRNA and *tetR* mRNA, which can only be translated when the suppressor tRNA concentration is sufficiently high. TetR then represses transcription of the T3RNAP gene, which eventually stops its own synthesis. Citrine and cerulean fluorescent proteins allowed us to simultaneously monitor expression from the two promoters in the system. A model of this genetic network (*SI Appendix*) produced oscillations using parameter estimates for the regulators involved. Modeling of this

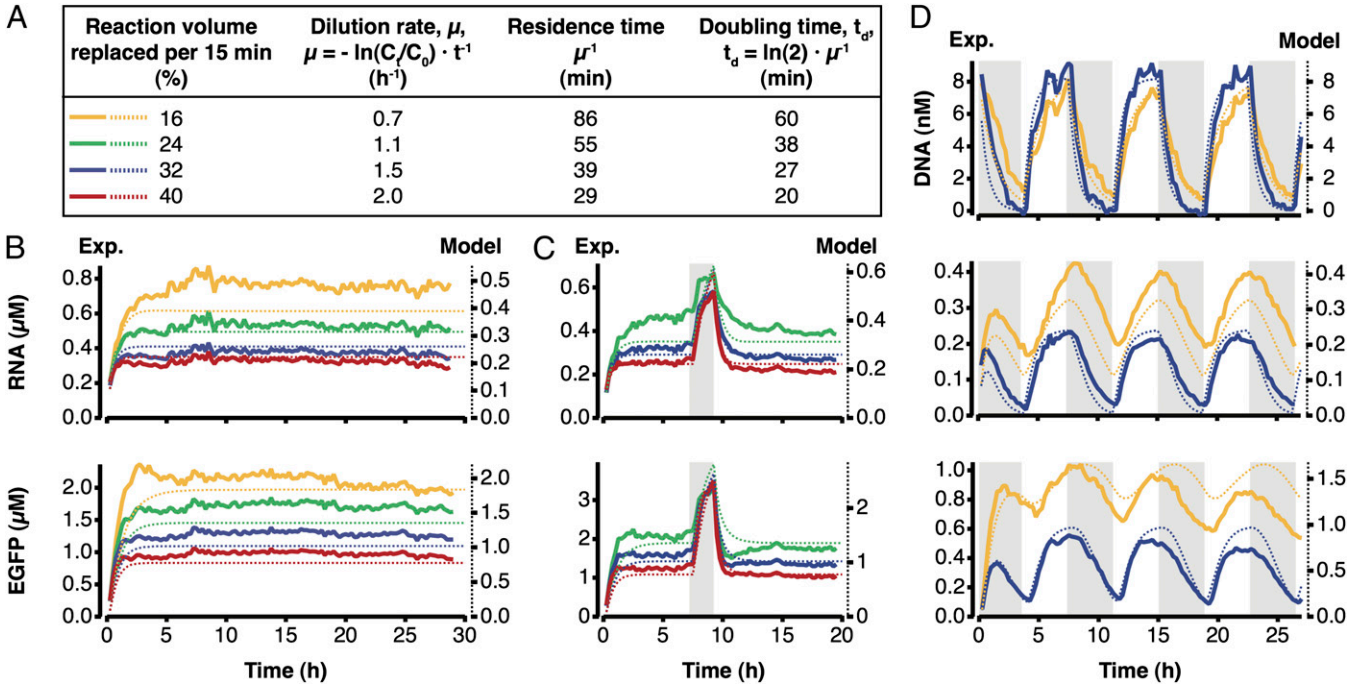

Fig. 2. Steady-state ITT. (*A*) Dilution conditions for the experiments in this figure. Experimental RNA and protein concentrations (solid lines, *Left* axes) and model prediction (dashed lines, *Right* axes) for (*B*) long-term ITT at different dilution rates, (*C*) a transient switch to batch conditions (shaded area), and (*D*) oscillating DNA template concentrations (shaded area, water added; white area, DNA added). DNA template concentration, 10 nM (*B* and *C*); maximum 8.2 nM (*D*).

system showed that the value of the dilution rate was critical for sustained oscillations to occur, which led us to test several dilution rates for each combination of DNA template concentrations. As expected, steady-state conditions were necessary to produce oscillations in our experiments and occurred only in a narrow range of dilution rates (Fig. 4*B*). The range of dilution rates that gave rise to oscillations increased with decreasing *supD* template concentration; *supD* was, however, necessary, as well as the other two components (*SI Appendix*, Fig. S3). For *supD* template concentrations below 82 nM, where oscillations were observed over a wider range of residence times, oscillation period increased linearly between 4 and 16 h as a function of residence time (*SI Appendix*, Fig. S4). These residence times correspond to cellular doubling times between 20 and 58 min. A similar dependence of period on dilution rate has been found for bacterial growth rates (29). Apart from oscillations or damped oscillations, two other general behaviors were observed: at high residence times reporter concentrations peaked once and then went to a low stable steady state, and at low residence times, or when *supD* template was absent, they immediately approached a stable steady state (Fig. 4*C* and *SI Appendix*, Fig. S5). The model of the oscillator produced similar results as a function of dilution rate (*SI Appendix*, Fig. S6) and was also able to capture the results of control experiments, where one network component at a time was removed from the system (*SI Appendix*, Figs. S3 and S7).

Discussion

Biological in vitro oscillations were previously achieved only in biochemically simple reactions, such as oligonucleotide-based systems containing an active degradation mechanism (1, 2). Our genetic oscillator shows that continuous reaction conditions allow complex dynamics to occur in cell-free protein synthesis reactions and in a sustained fashion. We observed that oscillations occurred in a narrow range of physiological dilution rates, which is important information for the implementation of in vivo oscillators, where dilution rates cannot be tuned as easily.

The examples of regulators we implemented in this study show that there appear to be no major limitations in the control mechanisms that can be implemented in vitro. Nonetheless, there are still many mechanisms to be tested, including different transcriptional repressors, transcriptional activators such as LuxR, or protein phosphorylation. Moreover, it may be possible to use systems that could not be implemented in vivo because of interference with vital processes in the host. In the course of characterizing different regulators with the goal of identifying suitable candidates to assemble a genetic oscillator, we found that *E. coli* RNA polymerase promoters recognized by σ^{70} often exhibited very low transcription rates. A recent report suggests that circular DNA might be a better template than linear DNA to reproduce in vivo transcription rates from *E. coli* promoters (30). To achieve tight repression of a strong promoter, we included two TetR operator sites into the T3 promoter, which explains its higher repression efficiency than the T7tet promoter. The TetR repressed version of the *E. coli* promoter featured two operator sites but the considerably lower activity in the unrepressed state made it less suitable for our oscillator design. The combination of transcriptional strength and tight repression are desirable features of promoters in many synthetic networks and often not trivial to engineer (25, 26). To achieve tighter control of the *tetR* gene in our oscillator network than transcriptional control could provide, we added stop codon suppression as a second regulatory level.

The reactor-based approach presented here allows bottom-up synthetic biology experiments to be performed in a completely defined and controlled environment. It differs from earlier designs of reactors for continuous ITT reactions (15, 17) in that it is not based on a size-exclusion membrane for exchange of molecules. In our microfluidic reactor-based approach, all molecules, including RNA polymerase, translation machinery, and DNA template, are constantly exchanged. Whereas the exchange

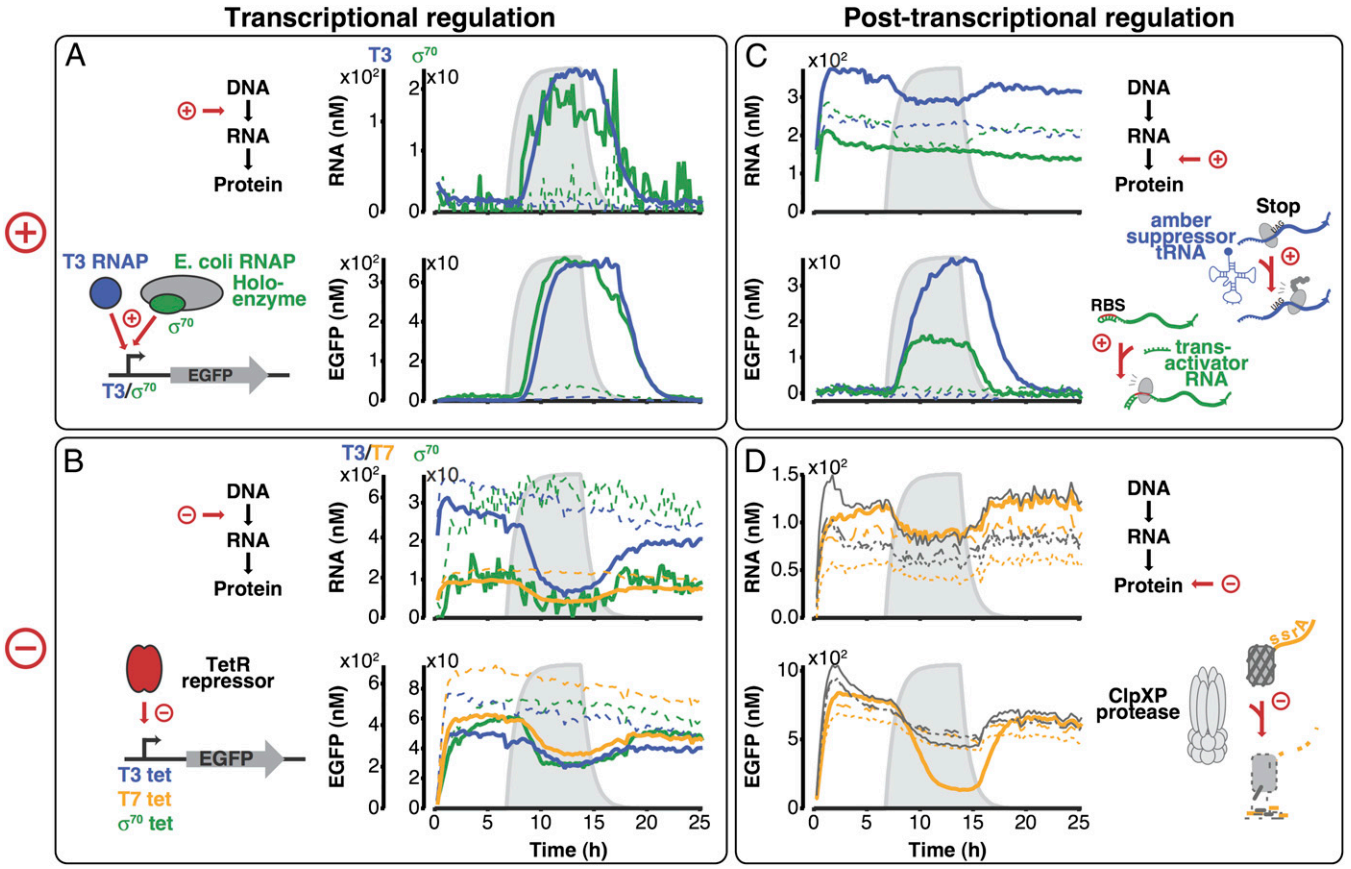

Fig. 3. Regulation at the transcriptional, translational, and posttranslational levels. Solid lines, experimental data; dashed lines, controls. DNA template of the regulator was transiently present (gray shaded area). Reporter (EGFP) DNA template was present at constant concentration. For a detailed summary of concentrations and controls, see *SI Appendix*, Table S2. (*A*) Transcriptional activation by T3RNAP and σ^{70}. *E. coli* RNAP core enzyme was present in the reaction mix. Controls: wrong activator. (*B*) Transcriptional repression by TetR. Promoters transcribed by three different RNA polymerases were tested in the presence of their respective polymerase. Controls: promoter without repressor binding site. (*C*) Activation of translation by RNA molecules. Controls: wrong activator. (*D*) Protein degradation by ClpXP protease. Controls: no degradation tag (ssrA), gray lines; only one protease subunit expressed, broken lines.

of enzymes involved in the reaction ensures that synthesis rates stay at a constant steady state even if they degrade over time, it could be interesting to immobilize the DNA templates in the reactor or to organize specific protein products in a spatial manner (31). Although our DNA template concentrations were in the range of low copy number plasmid concentrations in *E. coli*, RNA and protein concentrations were higher than average cellular concentrations. Due to the relatively large size of our nanoreactors (two orders of magnitude larger than the giant bacterium *Epulopiscium*) (32), stochastic processes may be difficult to study at the moment (33). It should however be feasible to scale down the 33-nL reactors by one to two orders of magnitude with existing microfabrication approaches (34) and to use *E. coil* RNAP instead of a phage RNAP. Down-scaling reactor volume would also permit hundreds to possibly thousands of reactors to be integrated on a single device (35, 36). Combined with high-throughput DNA synthesis methods (37) this approach would allow the rapid characterization of many synthetic network variants. Due to the fact that ITT reactions only require linear DNA templates, which were exclusively used in this study, such an in vitro screen would require no laborious cloning steps.

It will be exciting to determine whether any fundamental limits exist to the complexity of systems attainable in vitro. We were able to implement a genetic oscillator in vitro similar in complexity to synthetic gene networks achieved in vivo a few years ago (25). Our nanoreactor may prove to be a viable system to study processes that would interfere with vital processes in vivo or processes that occur in organisms that are unculturable. Furthermore, the system could be used to boot up and test the biochemical subsystems of a minimal artificial cell, including DNA replication (38), the translation machinery, or biosynthesis of precursors (39).

Methods

Preparation of DNA Templates. PCR for linear DNA templates was performed as previously described (22). Primer sequences are listed in *SI Appendix*, Table S1. PCR templates were pKT127 for EGFP (40), pKT211 for citrine (40), pBS10 for cerulean (Yeast Resource Center), BBa_K346000 (Registry of Standard Biological Parts) for T3 RNA polymerase, repressilator plasmid (25) for *tetR*, and *E. coli* DH5α genomic DNA for *rpoD*. Short DNA templates for *supD* (Registry of Standard Biological Parts; Part:BBa_K228001) and taR12 (26) were created by PCR using overlapping oligonucleotides. Regulatory sequences such as promoter, ribosomal binding site, terminator, and ssrA tag were included in the oligonucleotide primers. To monitor mRNA concentration, the EGFP template contained a target site for binary probes in its 3′ untranslated region (22). To monitor DNA concentration, the DNA template contained two Cy5 labels introduced by the 3′ and 5′ final primers.

Reaction Setup. We used the commercial PURExpress ITT kit (New England Biolabs) and added water to a volume of 80% of the final reaction volume. The remaining 20% of the reaction volume consisted of DNA template at five times its final concentration. ITT and DNA fractions were combined on the microfluidic chip. If necessary, the ITT mix was supplemented with binary probes (22) at a final concentration of 1 μM *E. coli* RNA polymerase core enzyme or holoenzyme (Epicenter) at 35 and 25 ng/μL, respectively, or 100 nM T3 RNAP polymerase (Fermentas). For a steady-state ITT reaction, ITT

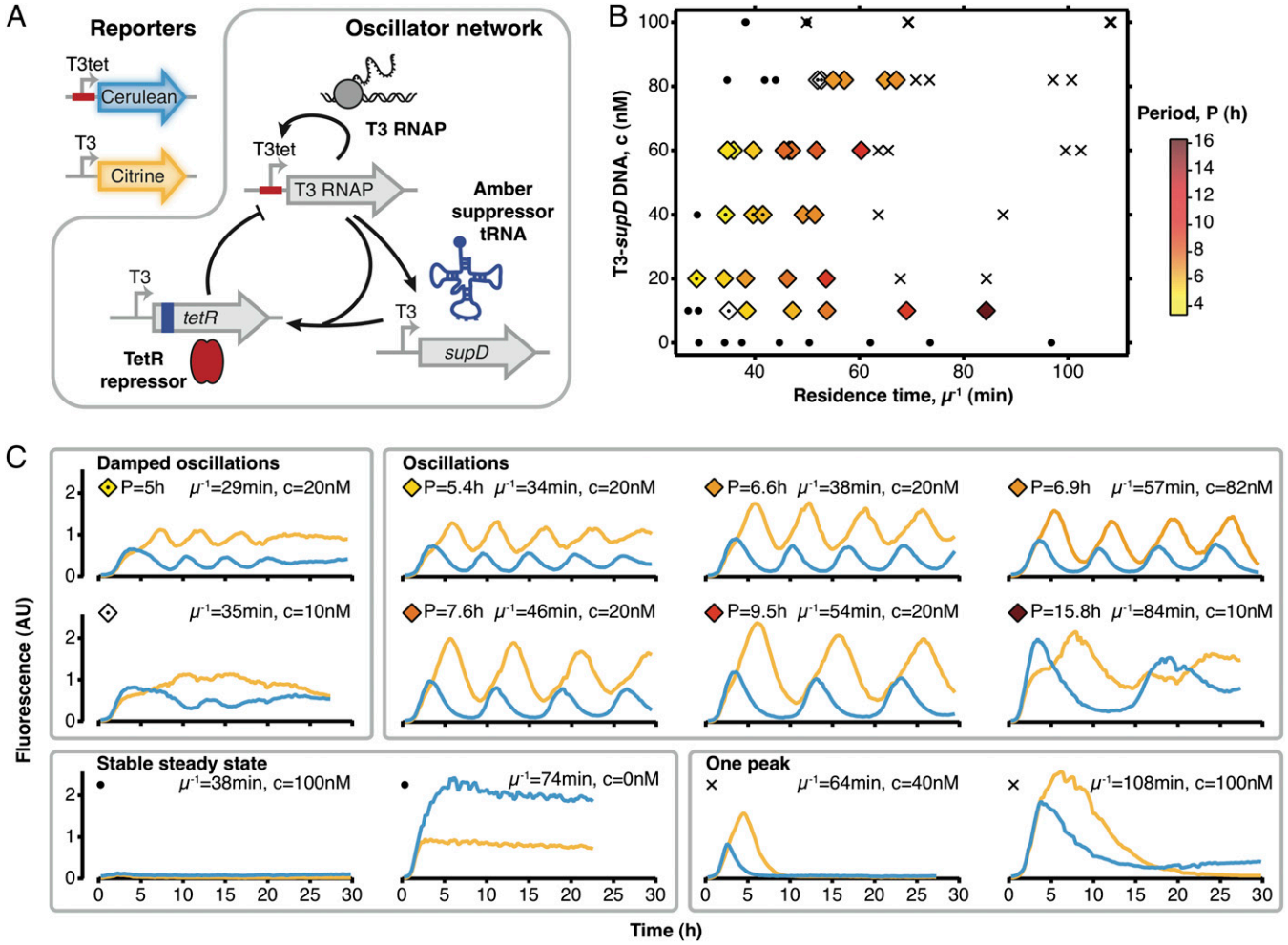

Fig. 4. Steady-state ITT conditions allow implementation of a genetic oscillator. (*A*) The oscillator network consists of three DNA templates: T3RNAP, *supD* amber suppressor tRNA, and TetR repressor. The TetR operator in the T3tet promoter and the amber stop codon in the *tetR* gene are indicated as red and blue boxes, respectively. Reporters for the two promoters in the network: yellow fluorescent protein (citrine) and cyan fluorescent protein (cerulean). (*B*) Phase diagram of the oscillator at different *supD* DNA template concentrations and different dilution rates. Oscillations (diamond symbols) occurred over a narrow range of dilution rates, which also determined the period of oscillations (fill color). Two other general behaviors were observed: one fluorescence peak and then low fluorescence (cross) or the system immediately reached a stable steady state (circles). (*C*) Cerulean (blue) and citrine (yellow) example traces.

mix and DNA were combined in the reactors on the microfluidic chip in a 5:1 ratio. Every 15 min, the reactor was imaged and a fraction of the reactor volume was replaced with fresh ITT mix and DNA at 5:1 ratio. Details on operation and characterization of the microfluidic chip can be found in the *SI Appendix*. Final concentrations of DNA templates in the genetic oscillator were 5 nM T3tet-T3RNAP, 10 nM T3-amber-*tetR*, and variable T3-*supD* concentration (between 0 and 100 nM). The reporter template DNAs for T3-citrine and T3-cerulean were at 2.5 nM each. Concentrations of DNA templates for the experiment with transcriptional and posttranscriptional regulators are summarized in *SI Appendix*, Table S2.

Data Acquisition and Analysis. We used an inverted microscope with an automated stage to image the eight reactors on the chip. Fluorescence was determined by imaging the reactor channel using a 20× magnification and fluorescence filters for GFP, Cy3-Cy5 FRET, Cy5, YFP, and CFP. Background fluorescence of a position next to the channel was subtracted from channel fluorescence. Concentrations of mRNA and EGFP were calculated from calibrations of FRET and EGFP fluorescence using purified molecules (22). To determine mRNA concentrations, we performed a blank reaction without DNA template in one of the reactors and subtracted FRET background fluorescence. Additionally, we normalized to average blank FRET fluorescence. To determine the period of sustained and damped oscillations of the genetic oscillator, we measured the time between the first and the second fluorescence maximum for both CFP and YFP fluorescence and used the average. Data were analyzed using IgorPro and MATLAB software.

Fabrication and Design of the Microfluidic Chip. Microfluidic devices were fabricated by standard multilayer soft lithography (41). Details on the design and operation of the chip are provided in *SI Appendix*.

ACKNOWLEDGMENTS. We thank José Garcia and Luis Fidalgo for helpful discussions. This work was supported by École Polytechnique Fédérale de Lausanne and a SystemsX.ch Grant DynamiX-RTD (2008/005).

1. Kim J, Winfree E (2011) Synthetic in vitro transcriptional oscillators. *Mol Syst Biol* 7:465.
2. Montagne K, Plasson R, Sakai Y, Fujii T, Rondelez Y (2011) Programming an in vitro DNA oscillator using a molecular networking strategy. *Mol Syst Biol* 7:466.
3. Loose M, Fischer-Friedrich E, Ries J, Kruse K, Schwille P (2008) Spatial regulators for bacterial cell division self-organize into surface waves in vitro. *Science* 320(5877):789–792.
4. Shimizu Y, et al. (2001) Cell-free translation reconstituted with purified components. *Nat Biotechnol* 19(8):751–755.
5. Noireaux V, Bar-Ziv R, Libchaber A (2003) Principles of cell-free genetic circuit assembly. *Proc Natl Acad Sci USA* 100(22):12672–12677.
6. Ishikawa K, Sato K, Shima Y, Urabe I, Yomo T (2004) Expression of a cascading genetic network within liposomes. *FEBS Lett* 576(3):387–390.

7. Isalan M, Lemerle C, Serrano L (2005) Engineering gene networks to emulate Drosophila embryonic pattern formation. *PLoS Biol* 3(3):e64.
8. Karig DK, Iyer S, Simpson ML, Doktycz MJ (2012) Expression optimization and synthetic gene networks in cell-free systems. *Nucleic Acids Res* 40(8):3763–3774.
9. Shin J, Noireaux V (2012) An E. coli cell-free expression toolbox: Application to synthetic gene circuits and artificial cells. *ACS Synth Biol* 1(1):29–41.
10. Xie Z, Liu SJ, Bleris L, Benenson Y (2010) Logic integration of mRNA signals by an RNAi-based molecular computer. *Nucleic Acids Res* 38(8):2692–2701.
11. Jewett MC, Calhoun KA, Voloshin A, Wuu JJ, Swartz JR (2008) An integrated cell-free metabolic platform for protein production and synthetic biology. *Mol Syst Biol* 4:220.
12. Davidson EA, Meyer AJ, Ellefson JW, Levy M, Ellington AD (2012) An in vitro autogene. *ACS Synth Biol* 1(5):190–196.
13. Shin J, Noireaux V (2010) Study of messenger RNA inactivation and protein degradation in an Escherichia coli cell-free expression system. *J Biol Eng* 4:9.
14. Spirin AS, Baranov VI, Ryabova LA, Ovodov SY, Alakhov YB (1988) A continuous cell-free translation system capable of producing polypeptides in high yield. *Science* 242(4882):1162–1164.
15. Spirin AS (2004) High-throughput cell-free systems for synthesis of functionally active proteins. *Trends Biotechnol* 22(10):538–545.
16. Khnouf R, Beebe DJ, Fan ZH (2009) Cell-free protein expression in a microchannel array with passive pumping. *Lab Chip* 9(1):56–61.
17. Siuti P, Retterer ST, Doktycz MJ (2011) Continuous protein production in nanoporous, picolitre volume containers. *Lab Chip* 11(20):3523–3529.
18. Noireaux V, Libchaber A (2004) A vesicle bioreactor as a step toward an artificial cell assembly. *Proc Natl Acad Sci USA* 101(51):17669–17674.
19. Hansen CL, Sommer MOA, Quake SR (2004) Systematic investigation of protein phase behavior with a microfluidic formulator. *Proc Natl Acad Sci USA* 101(40):14431–14436.
20. Ridgeway WK, Seitaridou E, Phillips R, Williamson JR (2009) RNA-protein binding kinetics in an automated microfluidic reactor. *Nucleic Acids Res* 37(21):e142.
21. Galas J-C, Haghiri-Gosnet AM, Estévez-Torres A (2013) A nanoliter-scale open chemical reactor. *Lab Chip* 13(3):415–423.
22. Niederholtmeyer H, Xu L, Maerkl SJ (2013) Real-time mRNA measurement during an in vitro transcription and translation reaction using binary probes. *ACS Synth Biol* 2(8): 411–417.
23. Karzbrun E, Shin J, Bar-Ziv RH, Noireaux V (2011) Coarse-grained dynamics of protein synthesis in a cell-free system. *Phys Rev Lett* 106(4):048104.
24. Stögbauer T, Windhager L, Zimmer R, Rädler JO (2012) Experiment and mathematical modeling of gene expression dynamics in a cell-free system. *Integr Biol (Camb)* 4(5): 494–501.
25. Elowitz MB, Leibler S (2000) A synthetic oscillatory network of transcriptional regulators. *Nature* 403(6767):335–338.
26. Isaacs FJ, et al. (2004) Engineered riboregulators enable post-transcriptional control of gene expression. *Nat Biotechnol* 22(7):841–847.
27. Anderson JC, Voigt CA, Arkin AP (2007) Environmental signal integration by a modular AND gate. *Mol Syst Biol* 3:133.
28. Banecki B, Wawrzynow A, Puzewicz J, Georgopoulos C, Zylicz M (2001) Structure-function analysis of the zinc-binding region of the Clpx molecular chaperone. *J Biol Chem* 276(22):18843–18848.
29. Stricker J, et al. (2008) A fast, robust and tunable synthetic gene oscillator. *Nature* 456(7221):516–519.
30. Chappell J, Jensen K, Freemont PS (2013) Validation of an entirely in vitro approach for rapid prototyping of DNA regulatory elements for synthetic biology. *Nucleic Acids Res* 41(5):3471–3481.
31. Heyman Y, Buxboim A, Wolf SG, Daube SS, Bar-Ziv RH (2012) Cell-free protein synthesis and assembly on a biochip. *Nat Nanotechnol* 7(6):374–378.
32. Mendell JE, Clements KD, Choat JH, Angert ER (2008) Extreme polyploidy in a large bacterium. *Proc Natl Acad Sci USA* 105(18):6730–6734.
33. Karig DK, Jung S-Y, Srijanto B, Collier CP, Simpson ML (2013) Probing cell-free gene expression noise in femtoliter volumes. *ACS Synth Biol*, 10.1021/sb400028c.
34. Thorsen T, Maerkl SJ, Quake SR (2002) Microfluidic large-scale integration. *Science* 298(5593):580–584.
35. Garcia-Cordero JL, Nembrini C, Stano A, Hubbell JA, Maerkl SJ (2013) A high-throughput nanoimmunoassay chip applied to large-scale vaccine adjuvant screening. *Integr Biol (Camb)* 5(4):650–658.
36. Rockel S, Geertz M, Hens K, Deplancke B, Maerkl SJ (2013) iSLIM: A comprehensive approach to mapping and characterizing gene regulatory networks. *Nucleic Acids Res* 41(4):e52.
37. Tian J, et al. (2004) Accurate multiplex gene synthesis from programmable DNA microchips. *Nature* 432(7020):1050–1054.
38. Fujiwara K, Katayama T, Nomura SM (2013) Cooperative working of bacterial chromosome replication proteins generated by a reconstituted protein expression system. *Nucleic Acids Res* 41(14):7176–7183.
39. Forster AC, Church GM (2006) Towards synthesis of a minimal cell. *Mol Syst Biol* 2:45.
40. Sheff MA, Thorn KS (2004) Optimized cassettes for fluorescent protein tagging in Saccharomyces cerevisiae. *Yeast* 21(8):661–670.
41. Unger MA, Chou HP, Thorsen T, Scherer A, Quake SR (2000) Monolithic microfabricated valves and pumps by multilayer soft lithography. *Science* 288(5463): 113–116.

Supplemental Material for

Implementation of cell-free biological networks at steady state

Henrike Niederholtmeyer, Viktoria Stepanova, and Sebastian J. Maerkl

This file includes:

Supplementary Figures S1-S18

Supplementary Tables S1-S2

Supplementary text

References (*1-11*)

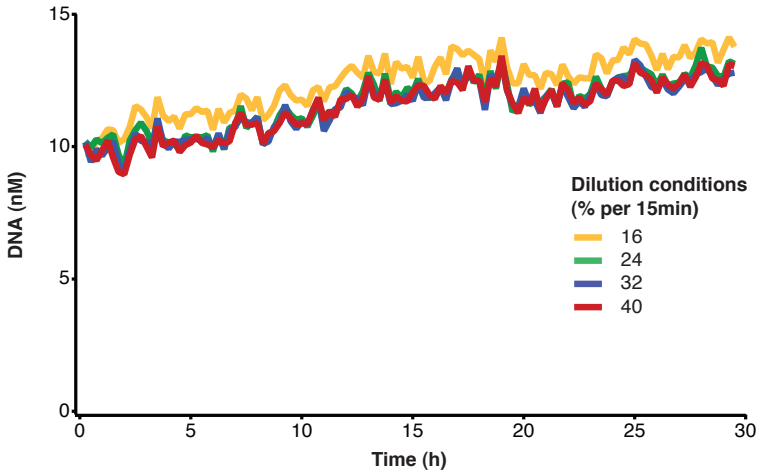

Fig. S1. DNA concentration during steady state ITT. DNA concentration during the steady state reaction at different dilution rates shown in Fig. 2B was monitored via Cy5 fluorescence of the labeled DNA template.

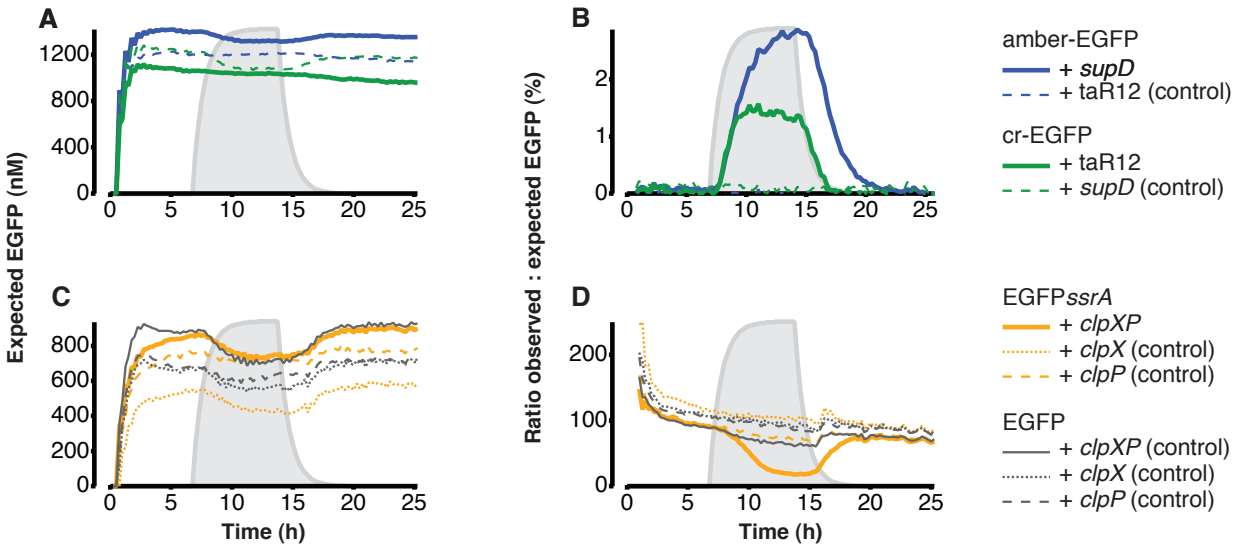

Fig. S2. Quantitative effects of post-transcriptional regulators. (**A**) Expected EGFP concentration calculated from measured mRNA concentrations for translational activation (Fig. 3C). (**B**) Ratio of observed to expected EGFP concentration, translation efficiency. (**C**) Expected EGFP concentration calculated from measured mRNA concentrations for protein degradation (Fig. 3D). (**D**) Ratio of observed to expected EGFP concentration to quantify the influence of protein degradation.

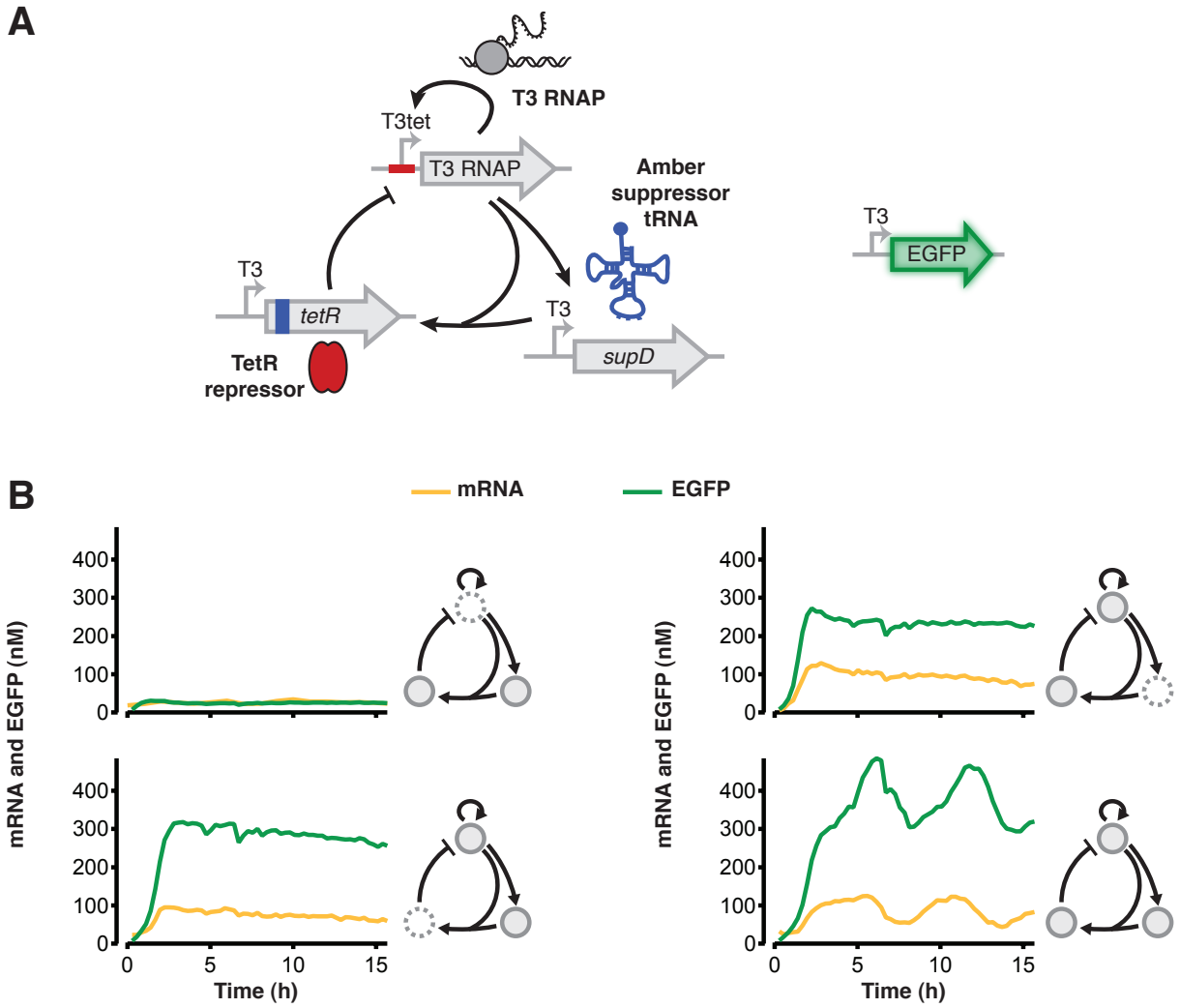

Fig. S3. Influence of the three oscillator genes. (**A**) Network design of the genetic oscillator. The TetR operator in the T3tet promoter and the amber stop codon in the *tetR* gene are indicated as red and blue boxes respectively. Concentrations of the oscillator DNA templates were 5nM T3tet-T3RNAP, 60nM T3-supD, 10nM T3-amber-tetR. We used the T3-EGFP reporter (5nM) with probe target site to determine mRNA concentration of the reporter during the reaction. (**B**) One network component was omitted at a time to determine if they were necessary to produce oscillations. Reactions were performed with a residence time of 49 min.

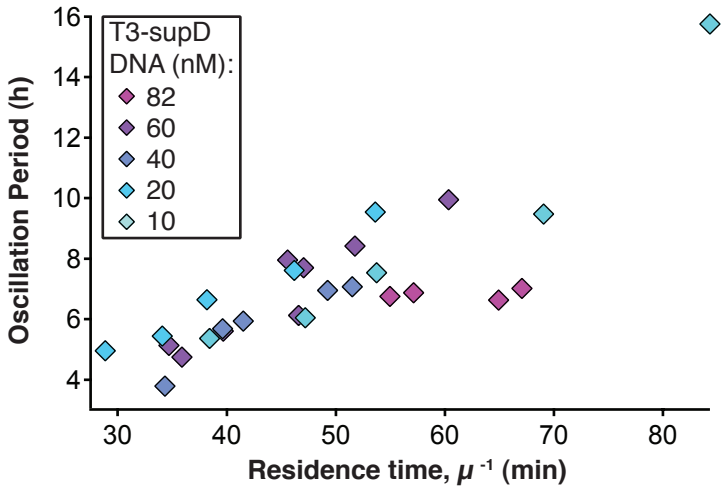

Fig. S4. Oscillation period versus residence time. Oscillation periods from experiments with different T3-*supD* DNA concentration (Figure 4) were plotted against residence time.

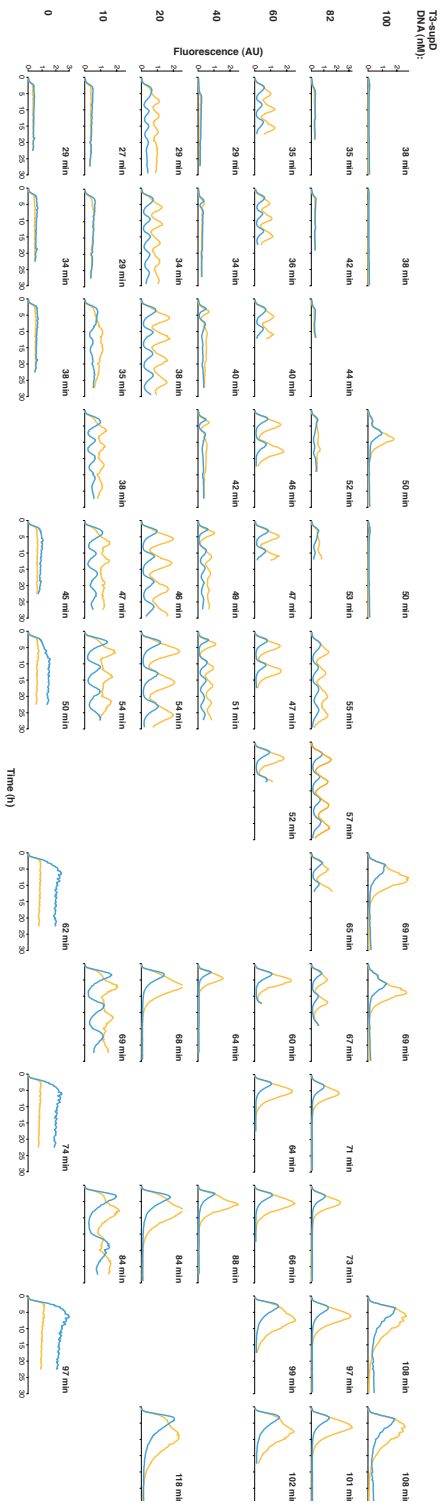

Fig. S5. Results of all oscillator experiments shown in Figure 4B. The graphs are ordered as in the phase diagram (Figure 4B) by T3-*supD* DNA concentration and residence time, which is noted for each graph in the top right.

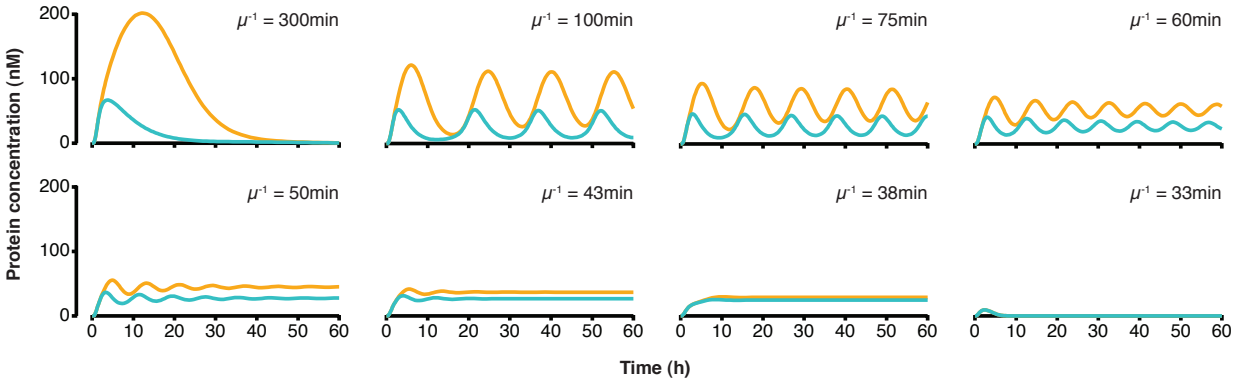

Fig. S6. Influence of dilution rate on oscillatory behavior of the model. Dilution rate, dil (μ), was varied in the model of the genetic oscillator (see SI text and Fig. 4A). Here, we show the concentrations of fluorescent Citrine (yellow lines) and fluorescent Cerulean (blue lines). For comparison to experimental results see Fig. 4 and Fig. S5.

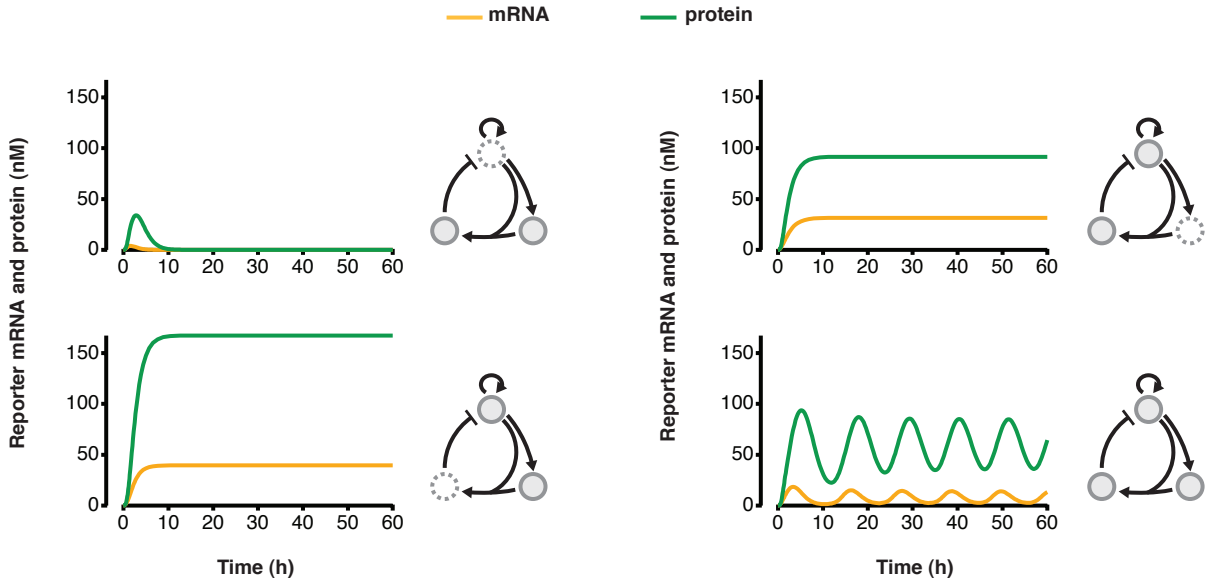

Fig. S7. Influence of the three oscillator genes in the model. The transcription rate of one oscillator gene at a time was set to 0 (top left $TXmax_{T3RNAP} = 0$, top right $TXmax_{supD} = 0$, bottom left $TXmax_{tetR} = 0$, bottom right all TXmax at default value). Reporter mRNA and protein of Citrine under control of the T3 promoter are shown. Dilution rate, dil, was set to $0.8h^{-1}$, which corresponds to a residence time of 75min. For comparison to experimental results see Fig. S3.

Table S1. Oligonucleotide primers used in the study.

Use and primer name	Sequence
Gene specific primers	
Color annotations: Ribosomal binding site Amber stop codon ssrA tag	
EGFP/Citrine-fwd	CCTCTAGAAATAATTTTGTTTAACTTAAGAAGGAGGAAAAAAAAATGTCTA AAGGTGAAGAATTATTCAC
amber-EGFP-fwd	CCTCTAGAAATAATTTTGTTTAACTTAAGAAGGAGGAAAAAAAAATGTAGA AAGGTGAAGAATTATTCACTG
EGFP/Citrine-rev	GTAGCAGCCTGAGTCGTTATTATTTGTACAATTCATCCATACCATGG
EGFP-ssrA-rev	GTAGCAGCCTGAGTCGTTATTAAGCAGCCAGAGCGTAGTTTTCGTCGTTAG CAGCTTTGTACAATTCATCCATACCATGG
T3RNAP-fwd	CCTCTAGAAATAATTTTGTTTAACTTAAGAAGGAGGAAAAAAAA ATGAACATCATCGAAAACATCG
T3RNAP-rev	GTAGCAGCCTGAGTCGTTA TTATGCAAAGGCAAAGTCAGAC
rpoD-fwd	CCTCTAGAAATAATTTTGTTTAACTTAAGAAGGAGGAAAAAAAA ATGGAGCAAAACCCGCAG
rpoD-rev	GTAGCAGCCTGAGTCGTTATTATTAATCGTCCAGGAAGCTACGC
tetR-fwd	CCTCTAGAAATAATTTTGTTTAACTTAAGAAGGAGGAAAAAAAAATGTCCA GATTAGATAAAAGTAAAG
amber-tetR-fwd	CCTCTAGAAATAATTTTGTTTAACTTAAGAAGGAGGAAAAAAAAATGTAGA GATTAGATAAAAGTAAAG
tetR-rev	GTAGCAGCCTGAGTCGTTATTAAGACCCACTTTCACATTTAAG
clpX-fwd	CCTCTAGAAATAATTTTGTTTAACTTAAGAAGGAGGAAAAAAAAATGACA GATAAACGCAAAGATG
clpX-rev	GTAGCAGCCTGAGTCGTTATTA TTCACCAGATGCCTGTTG
clpP-fwd	CCTCTAGAAATAATTTTGTTTAACTTAAGAAGGAGGAAAAAAAAATGTCAT ACAGCGGCGAAC
clpP-rev	GTAGCAGCCTGAGTCGTTATTAATTACGATGGGTCAGAATCGAATC
Cerulean-fwd	CCTCTAGAAATAATTTTGTTTAACTTAAGAAGGAGGAAAAAAAAATGAGTA AAGGAGAAGAACTTTTC
Cerulean-rev	GTAGCAGCCTGAGTCGTTATTATTTGTATAGTTCATCCATGCC
5' extension primers:	
Color annotations: Promoter tet operator	
5'ext-T7	GATCTTAAGGCTAGAGTACTAATACGACTCACTATAGGGAGACCACAACG GTTTCCCTCTAGAAATAATTTTGTTTAAC
5'ext-T7tet	GATCTTAAGGCTAGAGTACTAATACGACTCACTATAGGGAGATCTCCCTAT CAGTGATAGACCTCTAGAAATAATTTTGTTTAAC
5'ext-T3	GATCTTAAGGCTAGAGTACAATTAACACTCACTAAAGGGAGACCTCTAGAA ATAATTTTGTTTAAC

5'ext-T3tet	GATCTTAAGGCTAGAGTACTCCCTATCAGTGATAGAATTAACACTCACTAA AGGGAGATCCCTATCAGTGATAGACCTCTAGAAATAATTTTGTTTAAC
5'ext-σ^{70} lac	GATCTTAAGGCTAGAGTACAATTGTGAGCGGATAACAATTGACATTGTGAG CGGATAACAATATAATATGCGCATCCTCTAGAAATAATTTTGTTTAAC
5'ext-σ^{70} tet	GATCTTAAGGCTAGAGTACTCCCTATCAGTGATAGAGATTGACATCCCTAT CAGTGATAGATATAATATGCGCATCCTCTAGAAATAATTTTGTTTAAC

3' extension primers:
Color annotations: Terminator binary probe target

3'ext_no-tgt	CAAAAAACCCCTCAAGACCCGTTTAGAGGCCCCAAGGGGTTATGCTAGTTT TTTTTTTTTTTTTTTTTTTTTTTTTTGTAGCAGCCTGAGTCG
3'ext_3'tgt-3	CAAAAAACCCCTCAAGACCCGTTTAGAGGCCCCAAGGGGTTATGCTAGTTT TTTTTTTTTTTTTTTTTTTTTTTTTTGATAGAGTCCTTCCACGATACCAATGG GCTCAGTTTTTTGTTTTTTGGGTTTTGGTTTTGTTTTCCAGTACACAGGCGTA GCAGCCTGAGTCG

Final amplification primers:

5'final	GATCTTAAGGCTAGAGTAC or /Cy5/GATCTTAAGGCTAGAGTAC
3'final	CAAAAAACCCCTCAAGAC or /Cy5/CAAAAAACCCCTCAAGAC

Specialized primer sets:
Color annotations: Promoter Ribosomal binding site

supD:

T7-supD-fwd	GATCTTAAGGCTAGAGTACTAATACGACTCACTATAGGAGAGATGCCGGA GCGGCTGAACGGACCGGTCTC
T3-supD-fwd	GATCTTAAGGCTAGAGTACAATTAACACTCACTAAAGGAGAGATGCCGGA GCGGCTGAACGGACCGGTCTC
supD-rev	TGGCGGAGAGAGGGGGATTTGAACCCCCGGTAGAGTTGCCCCTACTCCGGT TTTAGAGACCGGTCCGTTCAGCCG

T7-cr-EGFP:

cr-EGFP-fwd (gene specific primer)	GGGTATTAAAGAGGAGAAAGGTACCATGTCTAAAGGTGAAGAATTATTCA C
5'ext-crR12-5' (upstream part of 5'ext)	GATCTTAAGGCTAGAGTACTAATACGACTCACTATAGGGAGAATTCTACCA TTCACC
5'ext-crR12-3' (downstream part of 5'ext)	GGTACCTTTCTCCTCTTTAATACCCAAATCCAAGAGGTGAATGGTAGAATT CTCCCT

T7-taR12:

T7-taR12-fwd	GATCTTAAGGCTAGAGTACTAATACGACTCACTATAGGACCCAAATCCAGG AGGTGATTGGTAG
taR12-rev	TCTAGAGATATATGGTAGTAGTAAGTTAATTTTCATTAACCACCACTACCA ATCACCTCCTGGATTTG

Table S2. DNA template concentrations for experiments in Figure 3. All reporter DNA templates contained a target site for binary probes to determine EGFP mRNA concentrations. DNA constructs are named by promoter name (see Table S1 for sequence) followed by a hyphen and the name of the controlled gene.

Experiment	Regulator DNA	Reporter DNA
Transcriptional activation (Figure 3A)		
by T3 RNA polymerase		
	1nM T7-T3RNAP	5nM T3-EGFP
control	1nM T7-rpoD	5nM T3-EGFP
by sigma factor 70 (σ^{70}, *rpoD*) in combination with *E. coli* RNA polymerase core enzyme		
	1nM T7-rpoD	10nM σ^{70}tet-EGFP
control	1nM T7-T3RNAP	10nM σ^{70}tet-EGFP
Transcriptional repression by TetR (Figure 3B)		
T7 RNA polymerase promoter		
	1nM T7-tetR	4nM T7tet-EGFP
control	1nM T7-tetR	4nM T7-EGFP
T3 RNA polymerase promoter		
	1nM T7-tetR	4nM T3tet-EGFP
control		
	1nM T7-tetR	4nM T3-EGFP
E. coli RNA polymerase σ^{70} promoter		
	1nM T7-tetR	4nM σ^{70}tet-EGFP
control	1nM T7-tetR	4nM σ^{70}lac-EGFP
Translational activation (Figure 3C)		
by amber suppressor tRNA (*supD*)		
	20nM T7-supD	10nM T7-amber-EGFP
control	20nM T7-taR12	10nM T7-amber-EGFP
by trans-activator RNA (taR12)		
	20nM T7-taR12	10nM T7-cr-EGFP
control	20nM T7-supD	10nM T7-cr-EGFP
Protein degradation by ClpXP (Figure 3D)		
of EGFP with degradation tag (ssrA)		
	2nM T7-clpX + 2nM T7-clpP	4nM T7-EGFP-ssrA
control	2nM T7-clpX	4nM T7-EGFP-ssrA
control	2nM T7-clpP	4nM T7-EGFP-ssrA
of EGFP without degradation tag		
control	2nM T7-clpX + 2nM T7-clpP	4nM T7-EGFP
control	2nM T7-clpX	4nM T7-EGFP
control	2nM T7-clpP	4nM T7-EGFP

Design and fabrication of the microfluidic chip

We designed a two-layer microfluidic chip to perform ITT reactions at steady state (Figure S8). The design of the microfluidic chip is similar to previous devices (1-3). One chip contains eight reaction rings to simultaneously run eight independent experiments. Different reagents can be connected to nine fluid inlets, which can be addressed by a multiplexer. Fluid bypasses allow rapid flushing of channels leading to the reaction rings. The inlet of each reaction ring can be opened and closed independently from the others. A peristaltic pump in front of the rings is used to meter reagents into the reaction rings. A second peristaltic pump is used to mix the contents inside the rings. The design allowed us to use different dilution rates or different template DNAs in each of the nanoreactors. Each nanoreactor had a volume of 33nL.

Molds for the control and the flow layer were fabricated on separate wafers by standard photolithography techniques and patterned with photoresist to produce channels with the heights stated in Figure S8. To ensure a homogenous film of photoresist on the mold for the flow layer, we applied the thinner AZ9260 first, and developed, before we spin-coated the thicker SU8 layer. The microfluidic chips were fabricated from PDMS by standard multilayer soft lithography (4). The control layer was located at the bottom of the chip and plasma bonded to a glass slide.

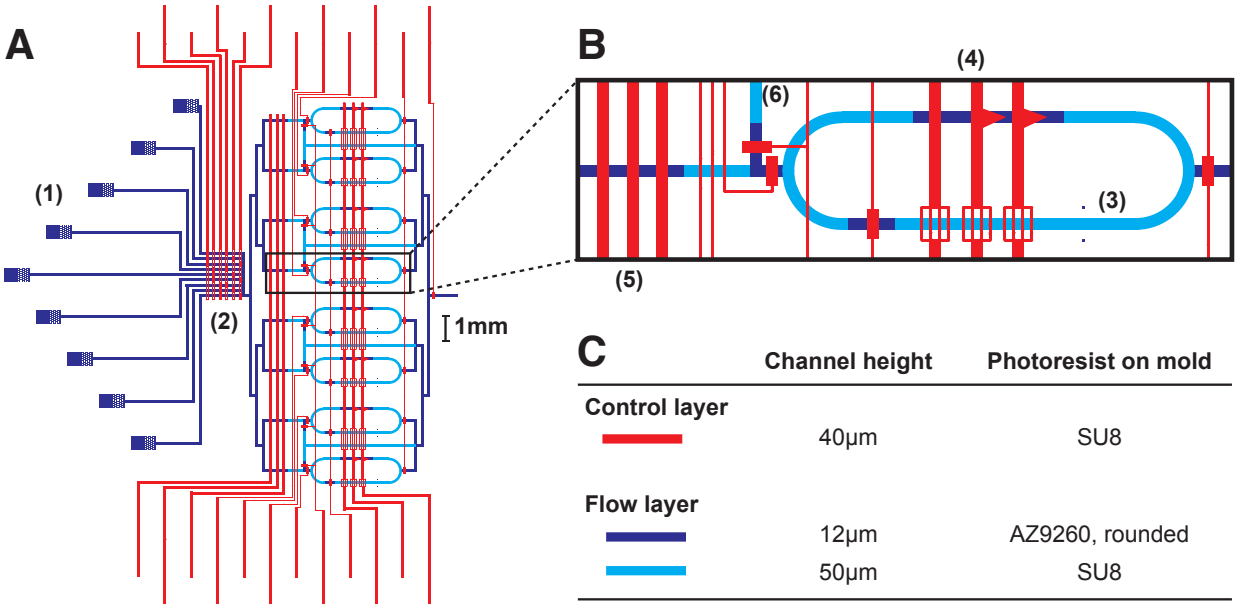

Fig. S8. Design of the microfluidic chip. (**A**) Design of the full microfluidic device. (**B**) Close-up of a reaction ring. The control layer is shown in red and the flow layer in two shades of blue. The width of a flow channel or a control valve is 100µm. (1) Reagent inlets, (2) multiplexer, (3) reaction ring and imaging position, (4) peristaltic pump for mixing of reagents in the reaction ring, (5) peristaltic pump to add reagents into the reaction ring, (6) bypass channel. (**C**) Channel heights and photoresists used.

Operation of the microfluidic chip

Pressure of microfluidic flow and control was regulated by a custom pneumatic setup. Control lines were set to 40psi, except the three lines, which controlled the peristaltic mixing pump, which were set to 20 psi using a separate pressure gauge and were additionally connected to a vacuum pump. Microfluidic valves were actuated by computer-controlled solenoid valves operated by a custom written LabView program. Depending on the experiment, flow pressure was regulated between 5 and 9psi to achieve additions between 0.4 and 1% of the ring volume per pump cycle. Usually, the flow pressure was set to the value where one pump cycle of the peristaltic input pump corresponded to 0.8% of the reactor volume.

The device was placed on an automated microscope in an opaque, temperature controlled incubation chamber, which allowed fluorescent imaging and a constant reaction temperature set to 37°C. One critical feature enabling long-term reaction conditions, was cooling of the ITT mixture before it enters the microfluidic chip, which was accomplished with a combination of a peltier element and water cooled heat sink (Figure S9). The volume of ITT mixture for the entire experiment was aspirated into a FEP (fluorinated ethylene propylene) tube, for storage on the peltier element. This tube was then connected to the microfluidic chip via a PEEK (polyether ether ketone) tube (Vici) with a thin inner diameter (180µm) to reduce the volume of un-cooled ITT reagent. For all other reagents we used tygon tubing without cooling.

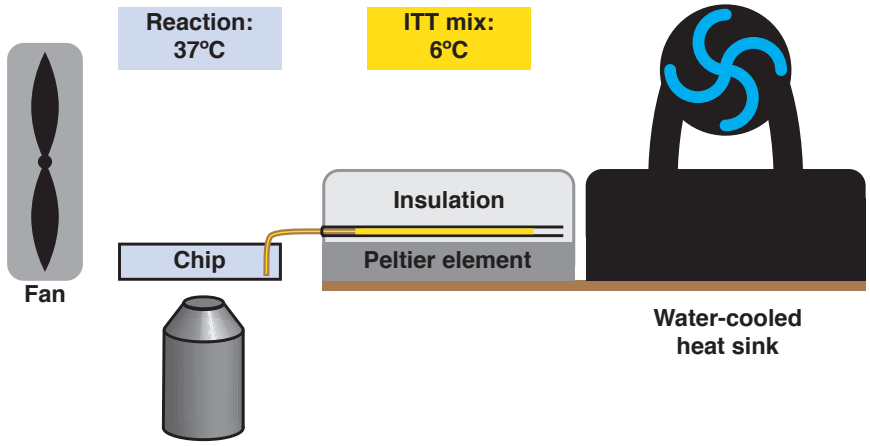

Fig. S9. Cooling of the ITT mix. Schematic of the custom-built cooling system for the ITT mix. The FEP tube holding the ITT mix for the experiment is held on top of a peltier element (Laird Technologies), it is connected to the microfluidic chip via a PEEK tube with a thin inner diameter (180µm). The heat sink for the peltier element is a copper plate cooled by a CPU cooler (EK waterblocks) connected to a water pump regulated to 8°C (Solid State cooling systems). In order to prevent condensation and ice formation on the edge of the peltier element facing the microfluidic chip, we placed a fan on the opposite site of the device. This temperature control system kept the ITT mix in the storage tube at approximately 6°C while the on-chip reaction temperature was 37°C, the temperature in the incubation chamber enclosing the setup.

Characterization of the microfluidic chip

The volume added into the reaction rings per pump cycle of the peristaltic input pump was consistent across the eight reactors on the chip and increased linearly with the number of pump cycles (Figure S10A). Before each experiment, the dilution rate was determined by measuring the washout rate of EGFP fluorescence (Figure S10B).

We measured the speed at which reagents inside the reaction rings were mixed by adding a plug of fluorescent EGFP solution into the rings. One position of the channel was imaged while the peristaltic pump started moving the fluorescent plug in a circle leading to mixing (Figure S11). Within less than 2 min mixing was completed.

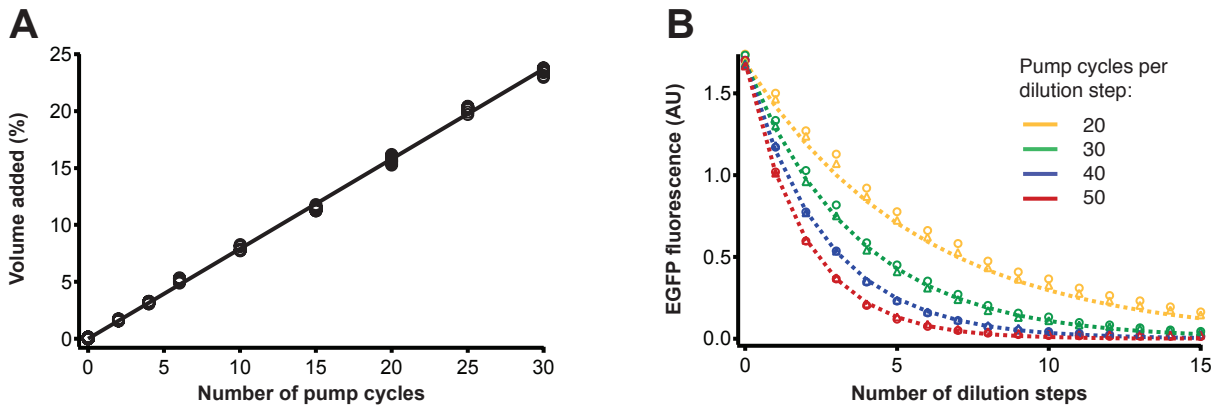

Fig. S10. Characterization of the peristaltic input pump. (**A**) Volume added into the reactors depends linearly on the number of pump cycles. Shown are the results from eight reactors of the same device. (**B**) Washout from the reactor at different dilution rates. Shown are the results of eight reactors from one device, with two repeats of each dilution rate (markers), and the prediction for a washout of 16, 24, 32 and 40% of reactor volume per dilution step (dashed lines). In both panels one pump cycle displaced 0.8% of the reactor volume.

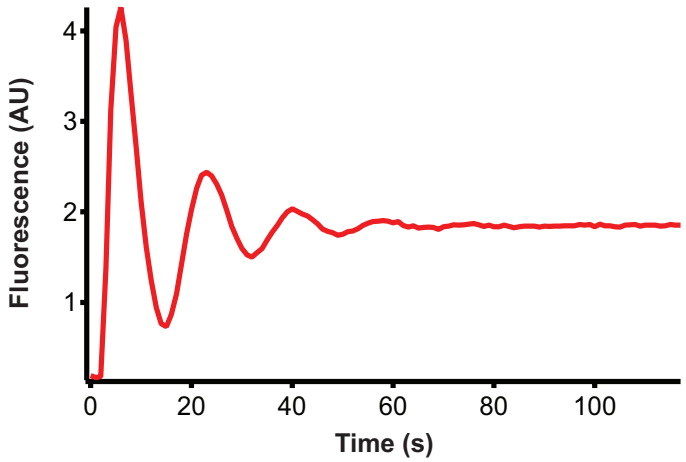

Fig. S11. Mixing of reagents in the reaction rings. To reaction rings filled with 2% BSA in PBS a plug of 7% of the reactor volume of 100µg/ml EGFP was added with the peristaltic input pump. The reactor channel was imaged while the peristaltic mixing pump moved the EGFP plug in a circle, causing the solutions to mix.

Experimental procedure

Priming and calibration
At the beginning of each experiment the device was primed with a solution of 2% BSA in PBS. Then, the dilution rates were calibrated as shown in Fig. S10B. This ensured correct functioning of the device before start of the experiment and to adjust the dilution rates to the desired value.

Steady state ITT reaction
Operation of the microfluidic chip and imaging during steady state ITT reactions was fully automated with a custom written LabView program. The sequence of operations was as follows:

Step	Operation
0	Initial fill: - flush reactors with ITT mixture - meter 20% reactor volume of template DNA into the reactors - mix
	Repeat the following steps every 15min:
1	Image each reactor
2	Flush the bypass channels with buffer
3	Addition of fresh ITT mix: - flush the bypasses channels with ITT mixture - add 4*n pump cycles of ITT mixture into the reactors - flush the bypass channels with buffer
4	Addition of DNA: - flush the bypasses channels with DNA solution - add n pump cycles of DNA into the reactors - flush the bypass channels with buffer
5	Mix
6	Repeat from step 1

Flushing of the bypass channels with costly reagents like ITT mixture and DNA solutions was done with the peristaltic input pump in order to reduce reagent consumption. For a complete experiment of 30h, only 6.25µl of ITT mixture were required per reactor. The buffer used for flushing was 5mM Tris-HCl pH8.5. The peristaltic mixing pump was actuated with a frequency of 8.3Hz. The input pump was actuated with a frequency of 1.7Hz for flushing the bypass channel, and with a frequency of 0.3Hz to add reagents into the reactions rings.

Rate measurements and model

Model of a batch ITT reaction

We describe the ITT reaction in batch with a set of six differential equations

DNA, *d*:
[1] $d'(t) = 0$

mRNA, *m*:
[2] $m'(t) = TX(d) \cdot act_{TX}(t) - \deg_m \cdot m(t)$

dark (immature) EGFP, p_d:
[3] $p_d'(t) = TL(m) \cdot act_{TL}(t) - mat \cdot p_d(t)$

fluorescent (mature) EGFP, p_f:
[4] $p_f'(t) = mat \cdot p_d(t)$

Relative transcriptional activity, act_{TX}:
[5] $act_{TX}'(t) = -\deg_{TX} \cdot act_{TX}(t)$

Relative translational activity, act_{TL}:
[6] $act_{TL}'(t) = -\deg_{TL} \cdot act_{TL}(t)$

We determined each parameter of this model in separate experiments. TX is the initial transcription rate that depends on DNA template concentration. TL is the initial translation rate that depends on mRNA concentration. We assume an unspecific decrease of those activities as a function of time and use act_{TX} and act_{TL} as the relative activities left at a given time. RNA, transcriptional activity and translational activity degrade/decrease with rates deg_m, deg_{TX}, deg_{TL} respectively. Dark EGFP matures to fluorescent EGFP with the rate *mat*. We did not observe any degradation of fluorescent EGFP.

Degradation of mRNA

The rate of mRNA degradation was determined as in (5) by monitoring the decrease of a known concentration of purified mRNA,m_0, in an on-chip batch reaction (Figure S12). The decreasing RNA concentration was fit to the solution of equation [2], with TX=0:

[7] $m(t) = m_0 \cdot e^{-\deg_m \cdot t}$

In different experiments and at different initial RNA concentrations we measured degradation rates between 0.003 and 0.008 min^{-1}. For the model, we used a RNA degradation rate deg_m of 0.003 min^{-1}.

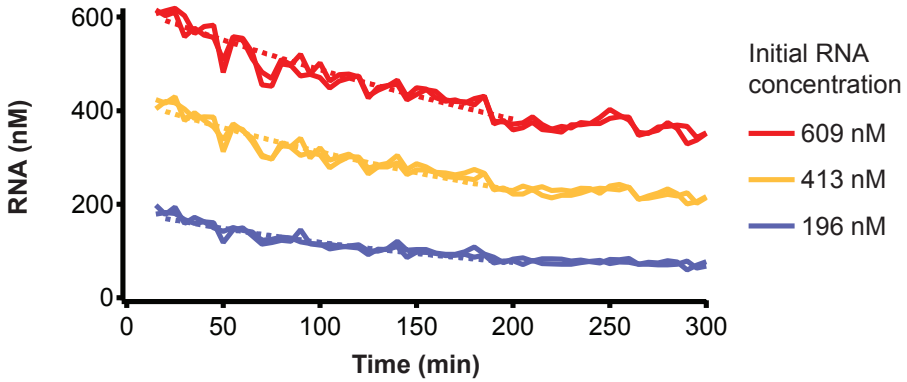

Fig. S12. Measurement of mRNA degradation rate. Different concentrations of purified mRNA were added to an ITT reaction on chip. Concentration of mRNA was monitored over time and fit to equation [7] (dashed lines).

Initial rate of transcription

We determined the initial transcription rate as a function of DNA in an on-chip batch reaction as in (5). The initial change in mRNA concentration can be described by equation [8] and we fit RNA concentration during the initial phase of the reaction to the solution, equation [9] (Figure S13A).

[8] $m'(t) = TX(d) - \deg_m \cdot m(t)$

[9] $m(t) = \frac{TX(d)}{\deg_m} \cdot (1 - e^{-\deg_m \cdot t})$

Transcription can be described by Michaelis-Menten kinetics:

[10] $TX(d) = \frac{TX_{\max} \cdot d}{K_{TX} + d}$

The maximal initial transcription rate, TX_{max}, was 11.5 nM/min and the DNA concentration for half maximal activity, K_{TX}, was 5.5nM (Figure S13B).

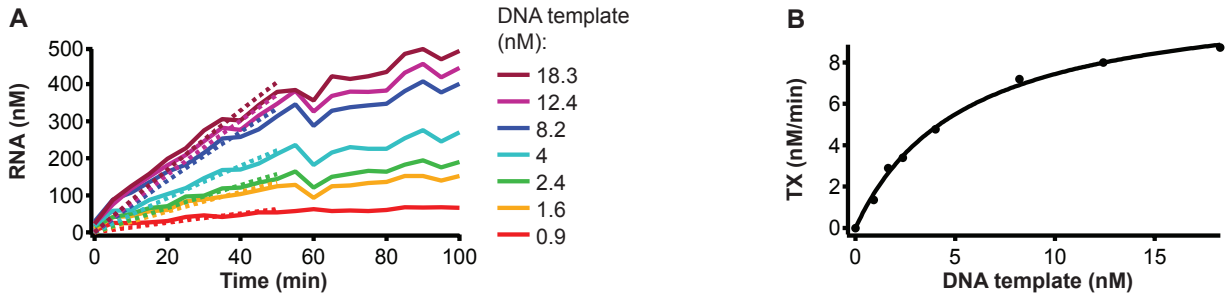

Fig. S13. Measurement of initial transcription rate. (**A**) RNA synthesis from different DNA template concentrations was monitored and the concentration during the initial 50 min of the reaction was fit to equation [9] using a fixed mRNA degradation rate, deg_m, of 0.003 min^{-1} (dashed lines) to determine TX(d). (**B**) Initial transcription rates as determined in (A) and fit to Michaelis-Menten kinetics (equation [10]).

Relative transcriptional activity over time

The relative transcriptional activity of an on-chip batch reaction over time was determined for RNA synthesis from different template DNA concentrations as in (5) using Euler's method (Figure S14):

[11] $m(t+\Delta t) = m(t) + (TX(d) \cdot act_{TX}(t) - \deg_m \cdot m(t)) \cdot \Delta t$

[12] $act_{TX}(t) = \dfrac{m(t+\Delta t) - m(t) + \deg_m \cdot m(t) \cdot \Delta t}{TX(d) \cdot \Delta t}$.

We approximated the mode of transcriptional activity decrease by exponential decay (see equation [5]). The rate of the decrease in relative transcriptional activity, $\deg_{TX}$, was on average 0.005 min^{-1}.

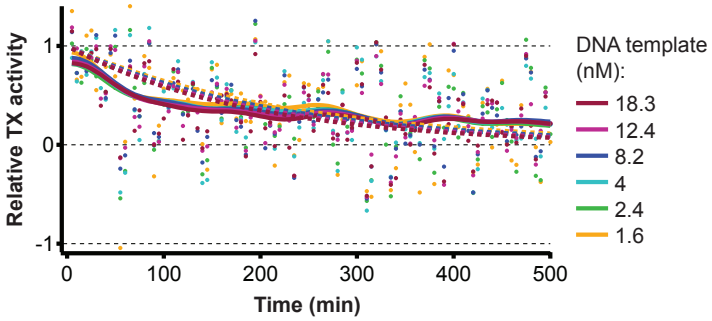

Fig. S14. Relative transcriptional activity over time. The relative transcriptional activity with respect to its initial value was calculated for RNA synthesis from different DNA template concentrations using equation [12] (dots) and the previously determined rates. These traces were smoothed for visualization (lines) and fit to an exponential decay function to determine the rate of decrease (dashed lines).

Maturation of EGFP

To determine the maturation rate of EGFP in our experimental conditions an ITT reaction producing EGFP was stopped by adding RNase, which immediately stops translation. Any increase of EGFP after this addition was therefore due to maturation of dark EGFP to fluorescent EGFP. This simplifies equation [3] to

[13] $p_d'(t) = -mat \cdot p_d(t)$

With this, the solution of equation (4) is:

[14] $p_f(t) = p_0 + \Delta p \cdot (1 - e^{-mat \cdot t})$

p_0 is the concentration of fluorescent EGFP when translation is stopped and Δp is the increase in its concentration when all dark EGFP is completely converted to fluorescent EGFP. EGFP maturation rate was determined to be 0.1 min^{-1} (Fig. S15).

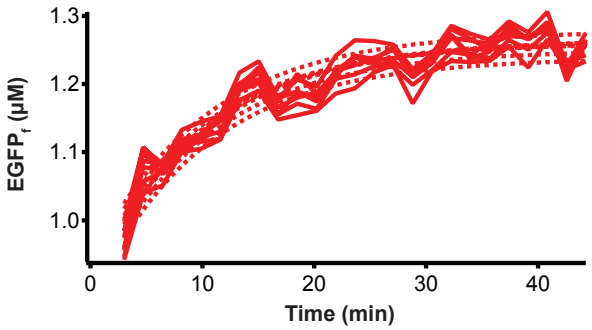

Fig. S15. Maturation of EGFP. After 25 min of an on-chip ITT reaction from a DNA template, translation was stopped by adding 0.6μM RNase. Concentration of fluorescent EGFP after RNase addition (lines) was fit to equation [14] to determine the maturation rate.

Initial rate of translation

We measured EGFP synthesis from different concentrations of purified mRNA. In the initial phase of this reaction, not taking into account a decrease of translational activity over time, this simplifies equations [2] and [3] to

[15] $m'(t) = -\deg_m \cdot m(t)$

[16] $p_d'(t) = TL(m) - mat \cdot p_d(t)$

With $TL(m) = \alpha_{TL} \cdot m(t)$ and $p_f(0)=p_d(0)=0$, the solution of equations [15], [16] and [4]:

[17] $p_f(t) = \frac{\alpha_{TL} \cdot m_0}{\deg_m \cdot (\deg_m - mat)} \cdot (mat \cdot (e^{-\deg_m \cdot t} - 1) + \deg_m \cdot (1 - e^{-mat \cdot t}))$.

Concentration of fluorescent EGFP of the initial phase of the reaction was fit to equation [17] to determine α_{TL} (Fig. S16A). Translation follows Michaelis-Menten kinetics:

[18] $TL(m) = \frac{TL_{max} \cdot m}{K_{TL} + m}$.

K_{TL}, the mRNA concentration at half-maximal translation rate, was determined from multiple benchtop experiments to be 150.2 nM. This K_{TL} was used to determine the average TL_{max} of two independent on-chip reactions. The TL_{max} on-chip was lower than in a benchtop reaction and also more variable (Fig S16B). For the model we used an average value of 76.4 nM/min.

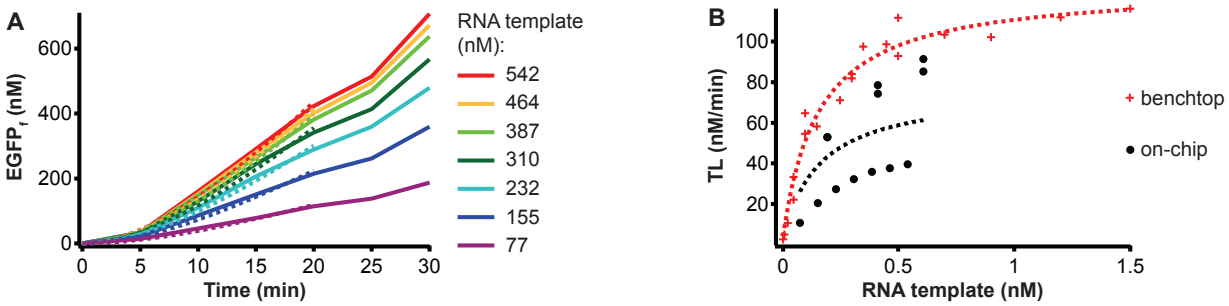

Fig. S16. Measurement of initial translation rate. (**A**) On-chip EGFP synthesis from different mRNA template concentrations was monitored and the concentration during the initial 20 min of the reaction was fit to equation [17] using the known initial mRNA concentration m_0 and the previously determined rates, $\deg_m$ and *mat* (dashed lines) to determine α_{TL}. (**B**) Initial transcription rates, TL, in a benchtop reaction (red crosses) and in two independent on-chip experiments (black circles) as determined in (A) were fit to Michaelis-Menten kinetics (equation [18]) (dashed lines).

Translational activity over time

Translational activity over time was determined by Euler's method. Equations [15], [3] and [4] can be written as

[19] $m(t+\Delta t) = m(t) - \deg_m \cdot m(t) \cdot \Delta t$

[20] $p_d(t+\Delta t) = p_d(t) + \Delta t \cdot (act_{TL}(t) \cdot TL(m) - mat \cdot p_d(t))$

[21] $p_f(t+\Delta t) = p_f(t) + \Delta t \cdot mat \cdot p_d(t)$.

From the known initial mRNA concentration, we calculated the mRNA concentration at each later time point. We had measured the concentration of fluorescent EGFP, p_f. Using smoothed p_f values we determined the concentration of dark EGFP, from equation [21]:

[22] $p_d(t) = \dfrac{p_f(t+\Delta t) - p_f(t)}{\Delta t \cdot mat}$.

This allowed us to calculate the relative translational activity, act_{TL} at each time point, which is the fraction of the initial activity left.

[23] $act_{TL}(t) = \dfrac{p_d(t+\Delta t) - p_d(t) + mat \cdot p_d(t) \cdot \Delta t}{\Delta t \cdot TL(m)}$.

Within one experiment the rate of decrease of translational activity was very consistent and did not depend on the mRNA concentration used (Fig. S17). The average rate of activity decrease determined from two independent on-chip experiments was 0.017min^{-1}.

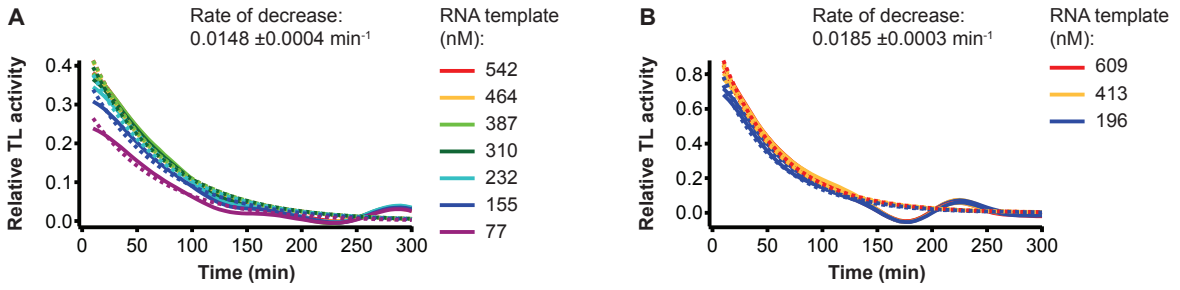

Fig. S17. Relative translational activity over time. In two independent on-chip experiments (**A** and **B**) EGFP was synthesized from different initial concentrations of purified mRNA. The relative translational activity with respect to its initial value was calculated using equations [19], [22], [23] and smoothed $EGFP_f$ measurement traces. The relative activities over time were then fit to an exponential decay function to determine the rate of decrease (dashed lines).

Summary of rates

The rates we measured here for a batch reaction on chip compared well with rates that were previously determined for the same ITT reaction mixture for bench-top reaction with larger volumes (5, 6). The following table summarizes all the rates we determined in the sections above that describe a batch reaction on chip, and that we used in our model:

Rate	**Value**
RNA degradation rate, deg_m	0.003 min^{-1}
Initial transcription rate, TX(d)	$TX(d)\frac{11.5\frac{nM}{\min}\cdot d}{5.5nM + d}$
Rate of relative transcriptional activity decrease, deg_{TX}	0.005 min^{-1}
EGFP maturation rate, *mat*	0.1 min^{-1}
Initial translation rate, TL(m)	$TL(m)\frac{76.4\frac{nM}{\min}\cdot m}{150.2nM + m}$
Rate of relative translational activity decrease, deg_{TX}	0.017 min^{-1}

Model of a continuous reaction with dilutions

To describe the continuous reaction in the microfluidic reactor we modeled the processes of the batch ITT reaction in discrete time intervals, Δt, of one minute. Every 15min a dilution fraction, *dil* (between 0.16 and 0.4, depending on the dilution conditions), was removed from the concentrations of the modeled molecules and the transcription and translation activities, which constitutes the washout. Also every 15min, full transcription and translation activities and DNA concentration, all scaled by fraction *dil*, were added:

		Every 15 min
DNA	$d(t+\Delta t) = d(t)$	$-dil \cdot d(t) + c \cdot dil \cdot d(t)$
mRNA	$m(t+\Delta t) = m(t) + \Delta t \cdot (TX(d) \cdot act_{TX}(t) - \deg_m \cdot m(t))$	$-dil \cdot m(t)$
EGFPd	$p_d(t+\Delta t) = p_d(t) + \Delta t \cdot (TL(m) \cdot act_{TL}(t) - mat \cdot p_d(t))$	$-dil \cdot p_d(t)$
EGFPf	$p_f(t+\Delta t) = p_f(t) + \Delta t \cdot mat \cdot p_d(t)$	$-dil \cdot p_f(t)$
Rel. TX act	$act_{TX}(t+\Delta t) = act_{TX}(t) - \Delta t \cdot \deg_{TX} \cdot act_{TX}(t)$	$-dil \cdot act_{TX}(t) + dil$
Rel. TL act	$act_{TL}(t+\Delta t) = act_{TL}(t) - \Delta t \cdot \deg_{TL} \cdot act_{TL}(t)$	$-dil \cdot act_{TL}(t) + dil$

Concentration, c, of DNA is usually equal to the initial DNA concentration d(0), in which case DNA concentration is constant. In special cases c can change transiently during the experiment, which leads to a new steady state DNA concentration, c.

Initial conditions

d(0) varied from experiment to experiment. In continuous ITT reactions $m(0)=p_d(0)=p_f(0)=0$ and $act_{TX}(0)=act_{TL}(0)=1$.

Prediction of transcriptional and translational activities at different dilution rates

The predicted relative transcriptional and translational steady state activities depended on the dilution rate. The higher the dilution rate, the higher was the steady state activity. Figure S18 shows the predicted relative transcriptional and translational activities for the experiments of Figure 2.

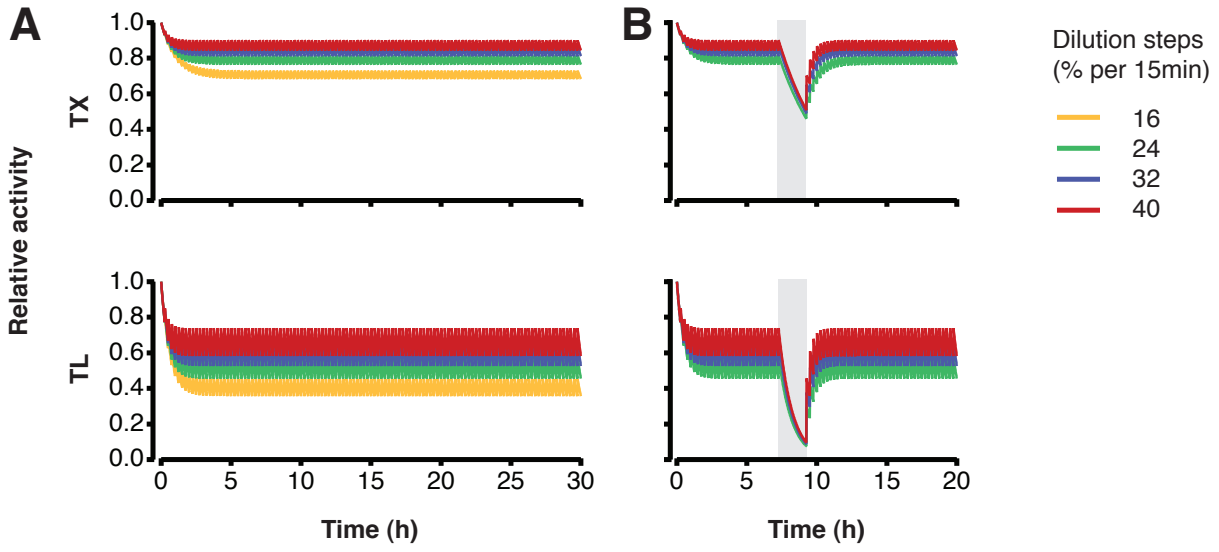

Fig. S18. Predicted relative transcriptional and translational activities at different reaction conditions. (**A**) Long-term steady state ITT at different dilution rates. The predicted relative transcriptional and translational activities shown here correspond to the experiment and predictions in figure 2B. (**B**) Transient switch to batch conditions. No dilutions occurred in the shaded time span. The predicted relative transcriptional and translational activities shown here correspond to the experiment and predictions in figure 2C. Relative activities were modeled with discrete dilution steps every 15min, which cause the teeth-like fluctuations.

Model of the repressilator in batch and continuous reaction

The repressilator consists of three transcriptional repressors, which each inhibit the expression of the preceding gene in the network (7). We modeled the repressilator as a symmetric system, where all repressors are identical except for their DNA-binding specifities, using the following differential equations for mRNA and protein concentration of the three repressors, R1-3 (i = R2, R3, R1 and j = R1, R2, R3):

$$m_i'(t) = act_{TX}(t) \cdot \frac{TX \cdot Km^n}{Km^n + p_j^n} - \deg_m \cdot m_i(t) - dil \cdot m_i(t),$$

$$p_i'(t) = act_{TL}(t) \cdot \frac{m_i(t)}{m_{total}(t)} \cdot TL(m_{total}(t)) - \deg_p \cdot p_i(t) - dil \cdot p_i(t).$$

We set the transcription rate at the unrepressed state, TX, of each promoter to 3nM/min, the Michaelis constant, Km, to 40nM and the Hill coefficient, n, to 2. The translation rate, TL, was calculated from equation 18. To take into account saturation of the translation machinery at high mRNA concentration we determined the translation rate for total mRNA concentration, m_{total}, and scaled by the fraction of mRNA concentration of the repressor modeled in that case.

Transcription and translation activities were modeled as above, using the following differential equations:

$$act_{TX}'(t) = -\deg_{TX} \cdot act_{TX}(t) - dil \cdot act_{TX}(t) + dil,$$

$$act_{TL}'(t) = -\deg_{TL} \cdot act_{TL}(t) - dil \cdot act_{TL}(t) + dil.$$

We compared behavior of the oscillator under batch and continuous reaction conditions. Additionally we modeled an "improved" batch reaction, where mRNA degradation and protein degradation rates are increased to *in vivo* levels of *E. coli* (8, 9), and where the rates of activity decrease of transcription and translation were a 10^{th} of the rates we measured. These improvements seem experimentally feasible, if mRNA and protein degradation mechanisms (8) and feeding of the ITT reaction by diffusion of small molecules (10, 11) were combined. The values of the following parameters were varied as follows in the three different reaction conditions:

	Reaction conditions		
Parameter	**Batch**	**Improved batch**	**Continuous**
Dilution rate, *dil*	0	0	$1.54h^{-1}$
mRNA degradation, deg_m	$0.003min^{-1}$	$0.053min^{-1}$	$0.003min^{-1}$
Protein degradation, deg_p	0	$0.017min^{-1}$	0
Decrease of transcriptional activity, deg_{TX}	$0.005min^{-1}$	$0.0005min^{-1}$	$0.005min^{-1}$
Decrease of translational activity, deg_{TL}	$0.017min^{-1}$	$0.0017min^{-1}$	$0.017min^{-1}$

Initial conditions were 1nM for all mRNA species, 0 for protein concentrations of R1 and R2 and 100nM of protein R3. Initial relative transcriptional and translational activities were 1. We show concentration of repressor protein R3 in Fig. 1E.

Model of the genetic oscillator built in this study

We modeled the genetic oscillator (see Fig. 4 for a diagram) with a set of 13 differential equations. We assume that general parameters of the ITT reaction are the same as determined for EGFP synthesis. Specifically, we use the same degradation rate, deg_m, for all RNA species as measured for EGFP mRNA, and the same translation rate TL. Also, decrease of transcriptional and translational activities were modeled as above, with the following two differential equations:

$$act_{TX}'(t) = -\deg_{TX} \cdot act_{TX}(t) - dil \cdot act_{TX}(t) + dil ,$$

$$act_{TL}'(t) = -\deg_{TL} \cdot act_{TL}(t) - dil \cdot act_{TL}(t) + dil .$$

RNA (m) synthesis from the TetR repressed T3tet promoter controlling the genes for T3RNAP and Cerulean were modeled by the following differential equations:

$$m_{\text{T3RNAP}}'(t) = act_{TX}(t) \cdot \frac{TX_{\text{T3RNAP}}(p_{\text{T3RNAP}}) \cdot K_{TetR}{}^{n}}{K_{TetR}{}^{n} + p_{TetR}{}^{n}} - \deg_m \cdot m_{\text{T3RNAP}}(t) - dil \cdot m_{\text{T3RNAP}}(t) ,$$

$$m_{\text{Cerulean}}'(t) = act_{TX}(t) \cdot \frac{TX_{\text{Cerulean}}(p_{\text{T3RNAP}}) \cdot K_{TetR}{}^{n}}{K_{TetR}{}^{n} + p_{TetR}{}^{n}} - \deg_m \cdot m_{\text{Cerulean}}(t) - dil \cdot m_{\text{Cerulean}}(t) ,$$

and RNA concentrations synthesized from unrepressed T3 promoter (*supD*, *tetR*, Citrine genes) were modeled with the following differential equations:

$$m_{\text{supD}}'(t) = act_{TX}(t) \cdot TX_{\text{supD}}(p_{\text{T3RNAP}}) - \deg_m \cdot m_{\text{supD}}(t) - dil \cdot m_{\text{supD}}(t) ,$$

$$m_{\text{tetR}}'(t) = act_{TX}(t) \cdot TX_{\text{tetR}}(p_{\text{T3RNAP}}) - \deg_m \cdot m_{\text{tetR}}(t) - dil \cdot m_{\text{tetR}}(t) \text{ and}$$

$$m_{\text{Citrine}}'(t) = act_{TX}(t) \cdot TX_{\text{Citrine}}(p_{\text{T3RNAP}}) - \deg_m \cdot m_{\text{Citrine}}(t) - dil \cdot m_{\text{Citrine}}(t) .$$

In all these RNA synthesis equations, transcriptional activation of the different genes by different concentrations of T3RNAP was described with:

$$TX_{gene}(p_{\text{T3RNAP}}) = \frac{TX\max_{gene} \cdot p_{\text{T3RNAP}}{}^{m}}{K_{\text{T3RNAP}}{}^{m} + p_{\text{T3RNAP}}{}^{m}} .$$

Changes in protein concentration, p, for T3RNAP, Citrine and Cerulean were modeled with the following differential equations. Like EGFP, Citrine and Cerulean have a dark and a fluorescent state, and we assume the same maturation rate (mat), as determined for EGFP:

$$p_{\text{T3RNAP}}'(t) = act_{TL}(t) \cdot \frac{m_{\text{T3RNAP}}(t)}{m_{total}(t)} \cdot TL(m_{total}(t)) - dil \cdot p_{\text{T3RNAP}}(t) ,$$

$$p_{\text{Cerulean}_d}'(t) = act_{TL}(t) \cdot \frac{m_{\text{Cerulean}}(t)}{m_{total}(t)} \cdot TL(m_{total}(t)) - mat \cdot p_{\text{Cerulean}_d}(t) - dil \cdot p_{\text{Cerulean}_d}(t),$$

$$p_{\text{Cerulean}_f}'(t) = mat \cdot p_{\text{Cerulean}_d}(t) - dil \cdot p_{\text{Cerulean}_f}(t),$$

$$p_{\text{Citrine}_d}'(t) = act_{TL}(t) \cdot \frac{m_{\text{Citrine}}(t)}{m_{total}(t)} \cdot TL(m_{total}(t)) - mat \cdot p_{\text{Citrine}_d}(t) - dil \cdot p_{\text{Citrine}_d}(t),$$

$$p_{\text{Citrine}_f}'(t) = mat \cdot p_{\text{Citrine}_d}(t) - dil \cdot p_{\text{Citrine}_f}(t).$$

For synthesis of TetR protein, stop codon suppression mediated by *supD* RNA had to be taken into account:

$$p_{tetR}'(t) = act_{TL}(t) \cdot \frac{m_{tetR}(t)}{m_{total}(t)} \cdot TL(m_{total}(t)) \cdot \frac{RT_{\max} \cdot m_{\sup D}(t)}{K_{\sup D} + m_{\sup D}(t)} - dil \cdot p_{tetR}(t).$$

Translation of each individual mRNA species was scaled to total (translated) mRNA, $m_{total} = m_{T3RNAP} + m_{tetR} + m_{Cerulean} + m_{Citrine}$.

We only have rough estimates of the individual parameters for transcription and translation of the different genes in the network as a function of their regulator concentrations. In the table below we list the values of the parameters that we used in the model to compare our experimental results (see below) and a reasonable range in which we think this value could differ (these estimates are based the results in Fig. 3, on our experience and initial experiments in batch format):

Parameter	**Value used in model**	**Probable range**
maximal transcription rates, $TXmax_{r,u}$ (at saturation T3RNAP concentration and unrepressed, and for the DNA template concentrations used in this study):		
$TXmax_{T3RNAP}$	7.5 nM/min	1 – 30 nM/min
$TXmax_{supD}$	20 nM/min	1 – 40 nM/min
$TXmax_{tetR}$	10 nM/min	1 – 30 nM/min
$TXmax_{Citrine,Cerulean}$	1 nM/min	0.2 – 10 nM/min
Michaelis-Menten constants (affinities) of TetR, T3RNAP and supD amber suppressor tRNA to their target sites:		
K_{tetR}	40 nM	20 – 500 nM
K_{T3RNAP}	500 nM	20 – 500 nM
K_{supD}	1000 nM	100 – 10 000 nM
Hill coefficients of TetR, T3RNAP and *supD* amber suppressor tRNA binding:		
for TetR: n	2	1 – 2
for T3RNAP: m	2	1 – 3
for *supD* (not modeled)	1	1 – 2
Maximal readthrough, stop codon suppression by supD amber suppressor tRNA (ratio of translated to untranslated mRNA):		
RT_{max}	0.5	0.001 – 0.9

Initial conditions were 25nM of T3RNAP mRNA and a transcriptional and translational activity of 1. Note that in our experiments it was not necessary to use an initial concentration of T3RNAP protein or mRNA, which was due to transcriptional leakage (leakage was not modeled here). Many parameter combinations in the probable range produced oscillations for broad ranges of feasible dilution rates. Generally, it was beneficial to have a low K_{tetR} value and medium to high transcription rates. The combination of parameters listed in the table above produced results that were very similar to our experimental observations but generally the oscillations had a longer period and occurred at slightly lower dilution rates than in the experiments. As in our experiments, we observed three different general behaviors as a function of dilution rate (Fig. S6). At low dilution rates we observed one peak of reporter proteins. At intermediate dilution rates we observed sustained or dampened oscillations, and at high dilution rates reporter protein concentrations stayed low. To reproduce the experiments shown in Fig. S3, we set the maximal transcription rates, TXmax, of one of the network components at a time to zero using a constant dilution rate that produced oscillations, when all network components were expressed. This resulted in the expected results that had also been observed in the experiment: no synthesis for $TXmax_{T3RNAP} = 0$; a stable steady state reporter synthesis for $TXmax_{supD} = 0$ and a slightly higher stable steady state reporter synthesis for $TXmax_{tetR} = 0$ (Fig. S7).

References:

1. Hansen CL, Sommer MOA, Quake SR (2004) Systematic investigation of protein phase behavior with a microfluidic formulator. *Proc Natl Acad Sci USA* 101:14431–14436.

2. Ridgeway WK, Seitaridou E, Phillips R, Williamson JR (2009) RNA-protein binding kinetics in an automated microfluidic reactor. *Nucleic Acids Res* 37:e142–e142.

3. Galas J-C, HAGHIRI-GOSNET A-M, Estévez-Torres A (2013) A nanoliter-scale open chemical reactor. *Lab Chip* 13:415–423.

4. Unger M, Chou H, Thorsen T, Scherer A, Quake S (2000) Monolithic microfabricated valves and pumps by multilayer soft lithography. *Science* 288:113.

5. Niederholtmeyer H, Xu L, Maerkl SJ (2012) Real-Time mRNA Measurement during an in Vitro Transcription and Translation Reaction Using Binary Probes. *ACS Synth Biol* 8:411-417.

6. Stögbauer T, Windhager L, Zimmer R, Rädler JO (2012) Experiment and mathematical modeling of gene expression dynamics in a cell-free system. *Integr Biol (Camb)* 4:494–501.

7. Elowitz MB, Leibler S (2000) A synthetic oscillatory network of transcriptional regulators. *Nature* 403:335–338.

8. Shin J, Noireaux V (2010) Study of messenger RNA inactivation and protein degradation in an Escherichia coli cell-free expression system. *J Biol Eng* 4:9.

9. Andersen JB et al. (1998) New unstable variants of green fluorescent protein for studies of transient gene expression in bacteria. *Appl Environ Microbiol* 64:2240–2246.

10. Noireaux V, Libchaber A (2004) A vesicle bioreactor as a step toward an artificial cell assembly. *Proc Natl Acad Sci USA* 101:17669–17674.

11. Shin J, Noireaux V (2012) An E. coli cell-free expression toolbox: application to synthetic gene circuits and artificial cells. *ACS Synth Biol* 1:29–41.